

# Investigating Multiple Solutions in the Constrained Minimal Supersymmetric Standard Model

---

B C Allanach,<sup>a</sup> Damien P. George<sup>a,b</sup> and Benjamin Nachman<sup>c</sup>

<sup>a</sup>*DAMTP, CMS, University of Cambridge, Wilberforce Road, Cambridge, CB3 0HA, U.K.*

<sup>b</sup>*Cavendish Laboratory, University of Cambridge, JJ Thomson Avenue, Cambridge, CB3 0HE, U.K.*

<sup>c</sup>*SLAC, Stanford University, 2575 Sand Hill Rd, Menlo Park, CA 94025, U.S.A.*

*E-mail:* [B.C.Allanach@damtp.cam.ac.uk](mailto:B.C.Allanach@damtp.cam.ac.uk), [dpg39@cam.ac.uk](mailto:dpg39@cam.ac.uk), [bnachman@cern.ch](mailto:bnachman@cern.ch)

ABSTRACT: Recent work has shown that the Constrained Minimal Supersymmetric Standard Model (CMSSM) can possess several distinct solutions for certain values of its parameters. The extra solutions were not previously found by public supersymmetric spectrum generators because fixed point iteration (the algorithm used by the generators) is unstable in the neighbourhood of these solutions. The existence of the additional solutions calls into question the robustness of exclusion limits derived from collider experiments and cosmological observations upon the CMSSM, because limits were only placed on one of the solutions. Here, we map the CMSSM by exploring its multi-dimensional parameter space using the *shooting method*, which is not subject to the stability issues which can plague fixed point iteration. We are able to find multiple solutions where in all previous literature only one was found. The multiple solutions are of two distinct classes. One class, close to the border of bad electroweak symmetry breaking, is disfavoured by LEP2 searches for neutralinos and charginos. The other class has sparticles that are heavy enough to evade the LEP2 bounds. Chargino masses may differ by up to around 10% between the different solutions, whereas other sparticle masses differ at the sub-percent level. The prediction for the dark matter relic density can vary by a hundred percent or more between the different solutions, so analyses employing the dark matter constraint are incomplete without their inclusion.

---

## Contents

<b>1</b>	<b>Introduction</b>	<b>1</b>
<b>2</b>	<b>Spectrum calculation in the CMSSM</b>	<b>3</b>
<b>3</b>	<b>RGE Solution Methods and Stability</b>	<b>6</b>
3.1	Fixed Point Iteration	6
3.2	The Shooting Method	8
<b>4</b>	<b>Numerical Procedure</b>	<b>10</b>
<b>5</b>	<b>Regions of Multiple Solutions</b>	<b>11</b>
5.1	Comparing algorithms	13
5.2	The LEP2 limit	15
5.3	The phenomenologically plausible strip	18
5.4	Example of Dark Matter Differences	21
5.5	Explorations in parameter space	21
<b>6</b>	<b>Summary and conclusions</b>	<b>25</b>
<b>A</b>	<b>Definition of Quantities in the Boundary Conditions</b>	<b>26</b>

---

## 1 Introduction

It has been recently discovered that for a given set of input parameters for the Constrained Minimal Supersymmetric Standard Model (CMSSM) [1–5], there can exist several distinct solutions for the particle spectrum [6]. This is because the renormalisation group equations (RGEs) connecting the high- and low-scale observables form a boundary value problem, which may admit multiple solutions. A priori, this fact has important consequences for experimental collider searches for new physics. Previous analyses that placed bounds on specific regions of the CMSSM parameter space used spectrum generators which missed the additional solutions. The published limits are therefore optimistic, as they ignore these additional, potentially viable solutions. We present here a study which shows that this initial cause of concern is not necessary for many sparticle searches: the phenomenology of the additional solutions are constrained by current and future experiments. However, there are particular cases (notably, those involving charginos), where care is needed and the additional solutions could provide a loop-hole to exclusion.

It was realised some years ago that the minimal supersymmetric standard model has an LHC inverse problem [7]. The problem is essentially that LHC observables possess degeneracies such that the Lagrangian of the MSSM cannot be uniquely determined from

them. It was thought though, that in strongly constrained set-ups like the CMSSM with only a few extra parameters and many potential LHC observables, that there would be no inverse problem (although even with fairly precise edge measurements, one could not always discriminate between minimal gauge mediated supersymmetry breaking patterns and the CMSSM [8]). Multiple solutions though, demonstrate that even the CMSSM has its ambiguities and suffers from the *opposite* of the LHC inverse problem. While the LHC inverse problem has several different parameter points leading to the same set of LHC observables, multiple solutions have the *same* CMSSM parameters leading to potentially *different* LHC observables. One must be careful to be aware of the multiple solutions so as to not rule out the model just because one is ignorant of an additional solution. The same caveat potentially applies to other models of SUSY breaking. This does not reintroduce the inverse problem, as sufficiently accurate observables will discriminate between the different solutions, since they are physically distinct.

The CMSSM is a model of softly broken supersymmetry (SUSY) that imposes many relations amongst the possible terms in the broken MSSM. In particular, at the Grand Unified Theory (GUT) scale, the scalar supersymmetric particles have the same mass  $m_0$ , the gauge fermion supersymmetric particles have the mass  $M_{1/2}$  and the trilinear scalar couplings (Higgs-sfermion-sfermion) are given by a new parameter  $A_0$  multiplied by the corresponding Standard Model Yukawa matrices. Additionally, the parameter  $\tan\beta$  specifies the ratio of the two Higgs' vacuum expectation values at the SUSY breaking scale. The final input to the CMSSM is the sign of the Higgsino mass term,  $\text{sign}(\mu)$ . The value of  $\mu$  is set by requiring the calculated  $Z^0$  mass is equal to the measured value (c.f. Eq. (A.1)). The SUSY particle spectrum at any given scale is then determined by solving the RGEs with boundary conditions at the three scales: GUT, SUSY breaking, and electroweak.

Specifying constraints at more than one scale creates a boundary value problem which, in general and in practice [6], can admit multiple solutions. This is different to the case where a single boundary condition has multiple solutions itself (see, for example the case of mSUGRA in Ref. [9], which gave up to three solutions for  $\tan\beta$ ). The existence of multiple solutions to the CMSSM RGEs for a given sign of  $\mu$  have evaded the standard SUSY spectrum generators such as SOFTSUSY [10], ISASUSY [11], SPheno [12], and SUSPECT [13]. The standard procedure for calculating supersymmetric spectra by all the current generators is fixed point iteration. This algorithm is blind to the extra solutions because they correspond to unstable fixed points — the standard methods move away from them by necessity. This fixed point iteration method can be modified, and partially improved, by choosing to *scan* over one of the dimensions of the RGE and also relax one constraint. For instance, one can scan the value of  $\mu$ , relax the condition on  $M_Z$ , and then investigate the locations in the one dimensional scan that give the correct prediction for  $M_Z(\text{exp})$ .

The more general method for finding all possible multiple solutions (at least within the available numerical precision and computing time) is to express the RGEs and the input data as an initial value problem. The Cauchy-Lipschitz theorem [14] states that this initial value problem has a unique solution provided the RGE trajectories are Lipschitz continuous (they are unless poles are encountered). For the CMSSM in the dominant third family

approximation<sup>1</sup>, one has 11 high-scale parameters to fix, and then runs the RGEs down to the lower scales to predict 11 quantities, most of which are Standard Model observables. The errors in the low-scale predictions are then used to formulate a root-finding problem: find the high-scale parameters that give negligible error for all predictions. We shall show in this paper how to implement this method using both the multidimensional Newton-Raphson and Broyden root finders. We then apply this general solver to well-studied slices of the CMSSM parameter space, to identify regions with multiple solutions and systematically study their phenomenology.

The paper is organised as follows. In Sec. 2 we review the calculation of the spectrum of the CMSSM, and how it is implemented in publicly available computer programs. Sec. 3 discusses the instability of fixed point iteration, and describes an alternative, the shooting method, which can be used to explore the full solution space of a model defined at multiple scales. The details of our numerics are given in Sec. 4. In Sec. 5 we present a map of multiple solutions in the CMSSM (for a few representative points in parameter space) and discuss the phenomenology of these solutions, giving limits based on collider and astrophysical data. Finally, Sec 6 summarises the work with a discussion on the impact of the multiple solutions on experimental exclusions.

## 2 Spectrum calculation in the CMSSM

To compute the observable spectrum of SUSY particles in the CMSSM one must determine the MSSM parameters in the model by solving their RGEs with certain boundary conditions. The high-scale boundary conditions of the CMSSM specify a theoretically motivated input on the soft supersymmetry-breaking mass terms in the Lagrangian, and the low-scale boundary conditions match parameters to known data on Standard Model fermion masses and mixings, gauge boson masses and gauge couplings. Over one hundred coupled, homogeneous, non-linear ordinary differential equations evolve the couplings between the different scales. At the high scale there are a certain number of fixed parameters (due to the GUT unification conditions) and the rest are initially free but must be solved for, such that all low scale constraints are satisfied. In this section we detail these boundary conditions and describe the existing method used to numerically compute solutions.

Boundary conditions are specified at three scales: the low scales  $M_Z$  and  $M_{\text{SUSY}}$ , and the high scale  $M_{\text{GUT}}$ . The latter two scales are part of the set of the free parameters and are themselves determined by the boundary conditions. The conditions at these scales are specified below, in terms of: the Yukawa couplings of the top, bottom, and tau, *viz.*  $h_t$ ,  $h_b$ , and  $h_\tau$ , respectively; the 3 MSSM gauge couplings,  $g_i$ ,  $i \in \{1, 2, 3\}$ ; the various SUSY breaking scalar masses,  $m_\varphi$ ; the gaugino masses,  $M_i$ ,  $i \in \{1, 2, 3\}$ ; and the SUSY breaking trilinear scalar couplings for top, bottom, and tau,  $A_t, A_b$  and  $A_\tau$ . Also included are constraints on the parameter  $\mu$  appearing in the superpotential<sup>2</sup>  $W \supset \mu \hat{H}_1 \hat{H}_2$ , and constraints on  $m_3^2$ , the parameter that mixes the two Higgs doublets in the potential  $V \supset$

<sup>1</sup>We shall work in the dominant third family approximation here, where the only Yukawa coupling entries that are non-zero are those in the (3, 3) position.

<sup>2</sup>The circumflex indicates a superfield.

$m_3^2 H_2 H_1$ . These latter two conditions (Eqs. (2.6),(2.7) below) come from the minimisation of the Higgs potential with respect to the neutral components of  $H_1$  and  $H_2$ . In terms of these variables the boundary conditions are

$$\tan \beta(M_Z) = \tan \beta(\text{input}), \quad (2.1)$$

$$h_t(M_Z) = \frac{m_t(M_Z)\sqrt{2}}{v(M_Z)\sin\beta}, \quad h_{b,\tau}(M_Z) = \frac{m_{b,\tau}(M_Z)\sqrt{2}}{v(M_Z)\cos\beta}, \quad (2.2)$$

$$v(M_Z) = 2\sqrt{\frac{M_Z(\text{exp})^2 + \Pi_{ZZ}^T(M_Z)}{\frac{3}{5}g_1^2(M_Z) + g_2^2(M_Z)}}, \quad (2.3)$$

$$g_1(M_Z) = g_1(\text{exp}), \quad g_2(M_Z) = g_2(\text{exp}), \quad g_3(M_Z) = g_3(\text{exp}), \quad (2.4)$$

$$M_{\text{SUSY}} = \sqrt{m_{\tilde{t}_1}(M_{\text{SUSY}})m_{\tilde{t}_2}(M_{\text{SUSY}})}, \quad (2.5)$$

$$\mu^2(M_{\text{SUSY}}) = \frac{m_{\tilde{H}_1}^2(M_{\text{SUSY}}) - m_{\tilde{H}_2}^2(M_{\text{SUSY}})\tan^2\beta(M_{\text{SUSY}})}{\tan^2\beta(M_{\text{SUSY}}) - 1} - \frac{1}{2}M_Z^2(M_{\text{SUSY}}), \quad (2.6)$$

$$\tan \beta(M_{\text{SUSY}}) = \tan \frac{1}{2} \left[ \sin^{-1} \left( \frac{2m_3^2(M_{\text{SUSY}})}{m_{\tilde{H}_1}^2(M_{\text{SUSY}}) + m_{\tilde{H}_2}^2(M_{\text{SUSY}}) + 2\mu^2(M_{\text{SUSY}})} \right) \right], \quad (2.7)$$

$$g_1(M_{\text{GUT}}) = g_2(M_{\text{GUT}}), \quad (2.8)$$

$$M_1(M_{\text{GUT}}) = M_2(M_{\text{GUT}}) = M_3(M_{\text{GUT}}) = M_{1/2}, \quad (2.9)$$

$$m_{\tilde{u}}^2(M_{\text{GUT}}) = m_{\tilde{d}}^2(M_{\text{GUT}}) = m_{\tilde{e}}^2(M_{\text{GUT}}) = m_{\tilde{L}}^2(M_{\text{GUT}}) = m_{\tilde{Q}}^2(M_{\text{GUT}}) = m_0^2 I_3, \quad (2.10)$$

$$m_{\tilde{H}_1}^2(M_{\text{GUT}}) = m_{\tilde{H}_2}^2(M_{\text{GUT}}) = m_0^2, \quad (2.11)$$

$$A_{\tilde{u}}(M_{\text{GUT}}) = A_0 I_3, \quad A_{\tilde{d}}(M_{\text{GUT}}) = A_0 I_3, \quad A_{\tilde{e}}(M_{\text{GUT}}) = A_0 I_3. \quad (2.12)$$

The running parameters in Eqs. (2.1)-(2.12) are in the modified dimensional reduction (DRED) scheme [15]. The ‘exp’ denotes that the value derives from experimental data. We have labelled the input parameter  $\tan\beta$  as  $\tan\beta(\text{input})$  to discriminate it from the predicted value run down from the GUT scale. The parameters  $m_{b,t,\tau}(M_Z)$  and  $g_{1,2,3}(M_Z)$  are obtained from experimental data, subtracting loops due to sparticles and Standard Model particles. The Standard Model electroweak gauge couplings  $g_1(\text{exp})$  and  $g_2(\text{exp})$  are fixed by the Fermi constant  $G_F$  and the fine structure constant  $\alpha$ . The values of  $g_i(\text{exp})$  are corrected by one-loop corrections involving sparticles. The parameter  $v(M_Z) \approx 246$  GeV denotes  $\sqrt{v_1^2(M_Z) + v_2^2(M_Z)}$ , where  $v_1$  and  $v_2$  are the vacuum expectation values of the neutral components of the Higgs doublets  $H_1$  and  $H_2$ , respectively. The modified DRED  $Z^0$  boson mass squared is fixed by  $M_Z^2(M_{\text{SUSY}}) = v^2(M_{\text{SUSY}}) (\frac{3}{5}g_1^2(M_{\text{SUSY}}) + g_2^2(M_{\text{SUSY}})) / 4$ . Furthermore,  $m_{\tilde{H}_i}^2 = m_{H_i}^2 - t_i/v_i$  are fixed by the soft SUSY breaking mass parameters for the Higgs fields  $m_{\tilde{H}_i}^2$ ,  $i \in \{1, 2\}$ , as well as by the tadpole contributions  $t_i$  coming from loops. These tadpole contributions have terms linear in  $\mu(M_{\text{SUSY}})$  as well as terms that are logarithmic in it, and so Eq. (2.6) is not a simple quadratic equation for  $\mu(M_{\text{SUSY}})$ . The symbol  $\Pi_{ZZ}^T(M_Z)$  denotes the MSSM self-energy correction to the  $Z^0$  boson mass which can be found in Ref. [16] and  $I_3$  is a  $3 \times 3$  matrix in family space. For further details, see the SOFTSUSY manual [10].

Spectrum calculators for the MSSM that are currently in the public domain, namely ISASUSY [11], SOFTSUSY [10], SPheno [12], SUSEFLAV [17] and SUSPECT [13], use fixed point

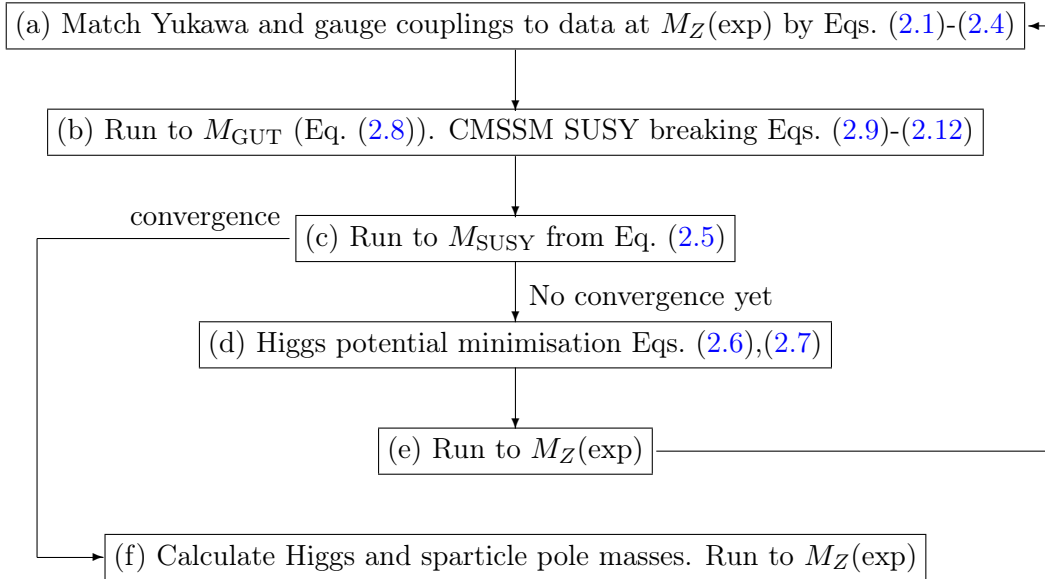


**Figure 1.** Fixed point iteration algorithm used by current publicly available SUSY spectrum calculators to calculate the SUSY spectrum. The initial step is the uppermost one.

iteration to find a self-consistent solution to Eqs. (2.1)-(2.12) (or equations very similar to them). The particular algorithm used by `SOFTSUSY`, for example, is shown in Fig. 1. The algorithm begins at  $M_Z$  by guessing values of all MSSM parameters at that scale. Threshold corrections to gauge and Yukawa couplings are calculated, and they are then matched to data including sparticle loop corrections. The MSSM parameters are then run to  $M_{\text{GUT}}$ , where the SUSY breaking equations are imposed. Running down to  $M_{\text{SUSY}}$ , parameters are fixed such that the Higgs potential gives the desired electroweak minimum. The MSSM parameters are then run back down to  $M_Z$ , where we return to point (a). This loop is continued until the MSSM parameters converge to within some fixed tolerance: i.e. running around the loop no longer changes them. When the algorithm finishes (point (c) in the figure), pole masses of Higgs' and sparticles are calculated.

This iterative algorithm is an example of fixed point iteration, where one attempts to find a set of values that remain invariant under application of a certain function. In the case at hand the values are the parameters of the MSSM and the function (actually a set of functions, one for each parameter) is one iteration of the loop in Fig. 1. If a solution to the system of MSSM RGEs is found then it is considered the one and only solution. Such an assumption is naïve, and it was shown in Ref. [6] that, due to the boundary value nature of the system, multiple solutions can, and do in fact, exist, depending upon CMSSM parameters. Amongst a set of multiple solutions, many of the  $M_{\text{GUT}}$  scale parameters (the ones that are set by the lower scale boundary conditions) are different, and so are many low-scale observables. Some are more different than others, however. The Higgs potential parameters  $\mu$  and  $m_3^2$  can be quite different between the different solutions.  $\mu$  changes the stop, sbottom and stau mixing. This then changes the top, bottom and tau Yukawa couplings at *leading log* order (i.e. first order in  $1/(16\pi^2) \log(M_{\text{GUT}}/M_Z)$ ), because

the measurement of the top, bottom or tau mass would include stop, sbottom or stau radiative corrections, respectively<sup>3</sup>. The fact that these couplings change then changes the RGE trajectories of most of the soft masses. Strictly speaking, these are only thus changed beyond leading log order (since it's a loop effect induced by an effect that is already leading log), but the large separation of scales between the weak and supersymmetry breaking scale can enhance the higher order logs.

Whilst fixed point iteration can in some cases use different starting conditions to find multiple solutions, we shall demonstrate in the next section that there are certain solutions which the algorithm can never converge on. We shall also show that such solutions are sometimes important in the context of CMSSM phenomenology.

### 3 RGE Solution Methods and Stability

In this section we first describe the potential non-robustness of fixed point iteration due to instabilities, and then detail a method of solving the multi-boundary problem that does not suffer from stability issues.

#### 3.1 Fixed Point Iteration

As mentioned in Sec. 2, current publicly available SUSY spectrum generators use *fixed point iteration* (FPI) to solve the multi-boundary problem relevant to the CMSSM. FPI operates by making a guess for the unknown high-scale parameters and repeatedly runs the RGEs down and up, applying the constraints until the solution no longer changes above some prescribed level. It has the distinct advantage of being very quick, as often only a few iterations are required in order to achieve convergence to some desired numerical accuracy. However, FPI generically suffers from stability issues: for a given point in parameter space, certain solutions may be unstable with respect to FPI, and so the algorithm will never converge on them. Here we review, following Ref. [18], the stability of FPI, first in the simple toy one-dimensional case, then generalising to the multi-dimensional case which is the case relevant for the CMSSM.

In one-dimension, FPI can be used to solve

$$x_* = f(x_*), \tag{3.1}$$

i.e.  $x_*$  represents a fixed point of the function  $f(x)$ . For FPI, we start with a guess  $x_1$  of the parameter, and generate (hopefully better) successive approximations by

$$x_{n+1} = f(x_n) \Leftrightarrow x_* - (x_* - x_{n+1}) = f(x_* - (x_* - x_n)). \tag{3.2}$$

Taylor expanding the right hand side around  $x_*$ , we have, to first order in  $x_* - x_n$ ,

$$\cancel{x_*} - (x_* - x_{n+1}) = \cancel{f(x_*)} - (x_* - x_n) \frac{df(x_*)}{dx} \Leftrightarrow (x_* - x_{n+1}) = (x_* - x_n) \frac{df(x_*)}{dx}. \tag{3.3}$$

---

<sup>3</sup>Neutralino and chargino masses and mixings are also affected, changing various radiative corrections (for example to the extracted electroweak gauge couplings). Thus, the electroweak gauge couplings also change to leading log order.



Stable convergence of FPI requires that, once  $x_n$  is sufficiently close to  $x_*$ , successive approximations are always closer:  $|x_* - x_{n+1}| < |x_* - x_n|$ . Therefore,

$$\left| \frac{df(x_*)}{dx} \right| < 1. \quad (3.4)$$

Conversely, if  $\left| \frac{df(x_*)}{dx} \right| > 1$ , then FPI will be unstable around the solution.

In our multi-dimensional case,  $\mathbf{x}$  represents MSSM couplings and masses, and  $\mathbf{f}(\mathbf{x})$  is the multi-dimensional function that represents what happens to  $\mathbf{x}$  after running up to the high scale, applying boundary conditions, running back down and applying the other boundary conditions, i.e. one iteration: the loop shown in Fig. 1. In the following, bold capitals represent matrices, whereas bold font lower case letters are vectors. We now have  $N$  fixed point equations

$$\mathbf{x}_* = \mathbf{f}(\mathbf{x}_*). \quad (3.5)$$

Proceeding similarly as we did in the one-dimensional case, we solve this system with successive approximations  $\mathbf{x}_n$ , where

$$\mathbf{x}_{n+1} = \mathbf{f}(\mathbf{x}_n) \Leftrightarrow \mathbf{x}_* - (\mathbf{x}_* - \mathbf{x}_{n+1}) = \mathbf{f}(\mathbf{x}_* - (\mathbf{x}_* - \mathbf{x}_n)). \quad (3.6)$$

Taylor expanding the right hand side around  $\mathbf{x}_*$ , we have, to first order in  $(\mathbf{x} - \mathbf{x}_n)$ ,

$$\cancel{\mathbf{x}_*} - (\mathbf{x}_* - \mathbf{x}_{n+1}) = \cancel{\mathbf{f}(\mathbf{x}_*)} - [(\mathbf{x}_* - \mathbf{x}_n)^T \cdot \nabla] \mathbf{f}|_{\mathbf{x}_*} \Leftrightarrow (\mathbf{x}_* - \mathbf{x}_{n+1}) = \mathbf{D}(\mathbf{x}_* - \mathbf{x}_n), \quad (3.7)$$

where  $\mathbf{D}$  is the *Jacobian matrix* of  $\mathbf{f}$ , evaluated at  $\mathbf{x}_*$ . Defining the *matrix norm*  $\|\mathbf{D}\|$  of  $\mathbf{D}$ ,

$$\begin{aligned} \|\mathbf{D}\| &\equiv \max_{\mathbf{x}: \|\mathbf{x}\|=1} \{ \|\mathbf{D}\mathbf{x}\| \} = \max_{\mathbf{x}: \mathbf{x} \neq \mathbf{0}} \left\{ \frac{\|\mathbf{D}\mathbf{x}\|}{\|\mathbf{x}\|} \right\} \\ \Rightarrow \|\mathbf{D}(\mathbf{x} - \mathbf{x}_n)\| &\leq \|\mathbf{D}\| \|\mathbf{x} - \mathbf{x}_n\|. \end{aligned} \quad (3.8)$$

Then Eq. (3.7) yields

$$\|\mathbf{D}\| < 1 \Rightarrow \|\mathbf{x}_* - \mathbf{x}_{n+1}\| < \|\mathbf{x}_* - \mathbf{x}_n\| \quad (3.9)$$

as a stability condition. Conversely, from Eq. (3.7), we have

$$\min_{\mathbf{x}: \|\mathbf{x}\|=1} \{ \|\mathbf{D}\mathbf{x}\| \} > 1 \Rightarrow \|\mathbf{x}_* - \mathbf{x}_{n+1}\| > \|\mathbf{x}_* - \mathbf{x}_n\|. \quad (3.10)$$

If Eq. (3.10) is satisfied, the solution is clearly unstable to FPI<sup>4</sup>. Depending upon CMSSM parameters then, there may be solutions to the RGEs that have not been found by publicly available spectrum calculators, all of which rely on FPI. This was demonstrated to be true in Ref. [6], where one of the boundary conditions (Eq. (2.6)) was inverted:  $\mu(M_{\text{SUSY}})$  was fixed, and the equation was used instead to predict  $M_Z$ . It was demonstrated that some points in CMSSM parameter space had *several different* values of  $\mu(M_{\text{SUSY}})$  that fit the empirically measured central value for  $M_Z$  i.e.  $M_Z(\text{exp})$ . These constituted multiple solutions of the RGEs for the same CMSSM point. Running FPI on some of the additional solutions showed that they were unstable, with parameters getting successively further from the solution in question.

---

<sup>4</sup>Note that there could also be solutions for which neither Eq. (3.9) nor Eq. (3.10) are true. For such solutions, it is unclear what the stability properties would be.



$V_1 = \tan \beta(M_{\text{GUT}})/10$	$V_7 = Y_t(M_{\text{GUT}})$
$V_2 = \ln(M_{\text{GUT}}/1 \text{ GeV})$	$V_8 = Y_b(M_{\text{GUT}})$
$V_3 = g_1(M_{\text{GUT}})$	$V_9 = Y_\tau(M_{\text{GUT}})$
$V_4 = g_3(M_{\text{GUT}})$	$V_{10} = v(M_{\text{GUT}})/1000 \text{ GeV}$
$V_5 = [\mu(M_{\text{GUT}})/1000 \text{ GeV}]^2$	$V_{11} = M_{\text{SUSY}}(M_{\text{GUT}})/1000 \text{ GeV}$
$V_6 = m_3^2(M_{\text{GUT}})/10^6 \text{ GeV}^2$	

**Table 1.** Dimensionless order one input variables for each CMSSM point.

### 3.2 The Shooting Method

The *shooting method* [19] provides an alternative method to FPI of solving a multi-boundary problem. Instead of running the RGEs up and down, one runs only in one direction, by first applying the boundary conditions relevant for the starting scale and guessing any parameters that are not fixed by these boundary conditions. It is convenient for us to start at  $M_{\text{GUT}}$ , applying the boundary conditions found in Eqs. (2.8)-(2.12). When one runs to the other scale (in our case  $M_{\text{SUSY}}$  then the weak scale), in general the other boundary conditions are not exactly satisfied. One keeps on adjusting the values of the guessed GUT scale parameters until, after running down, all of the  $M_{\text{SUSY}}$  and weak-scale boundary conditions are satisfied to some prescribed numerical accuracy.

We now face the fact that to truly have a chance of numerically finding all of the solutions, we must hunt in eleven dimensions for each CMSSM point. That is, for each choice of  $m_0$ ,  $M_{1/2}$ ,  $A_0$ ,  $\tan \beta$  and  $\text{sgn}(\mu)$ , specifying a point in the CMSSM parameter space, there are 11 high-scale parameters (to be detailed below) which must be determined such that the low-scale constraints are satisfied. The overall strategy is to start at the high scale  $M_{\text{GUT}}$ , input the MSSM parameters  $y_i$ , consistent with  $M_{\text{GUT}}$ -scale CMSSM boundary conditions, and evolve the RGEs down to  $M_{\text{SUSY}}$  where the electroweak symmetry breaking boundary conditions should be met, then to the weak scale, where various weak-scale boundary conditions should be met.

The MSSM renormalisation group equations may be phrased in general as

$$\frac{dy_i}{dt} = h_i(y_1, y_2, \dots, y_N), \quad (3.11)$$

where,  $i \in \{1, 2, \dots, 109\}$  and  $t = \ln(Q/\text{GeV})$ ,  $Q$  being the modified dimensional reduction scheme [15] renormalisation scale, in units of GeV. The  $h_i$  are in general non-linear functions of the relevant MSSM parameters  $y_i$ . Here, for a given CMSSM point, we have the dimensionless  $\sim \mathcal{O}(1)$  input parameters displayed in Table 1. Eqs. (2.8)-(2.12) are applied upon all of the soft SUSY breaking terms, and the MSSM couplings and parameters are evolved from  $Q/\text{GeV} = \exp(V_2)$  to  $Q/\text{GeV} = 1000V_{11}$ .

We wish to find values of the  $V_i$  such that the boundary conditions at  $M_{\text{SUSY}}$  and  $M_Z$  are satisfied:

$$f_i(V_1, V_2, \dots, V_{11}) = 0, \quad (3.12)$$

where the definitions of the  $f_i$  are shown in Table 2. Thus, we must adjust the 11  $V_i$

$f_1 = M_Z(\text{pred})^2/M_Z(\text{exp})^2 - 1$	$f_2 = \tan \beta(M_{\text{SUSY}})/\tan \beta^{\text{pred}}(M_{\text{SUSY}}) - 1$
$f_3 = M_{\text{SUSY}}/M_{\text{SUSY}}^{\text{pred}} - 1$	$f_4 = Y_t^{\text{pred}}(M_Z(\text{exp}))/Y_t(M_Z(\text{exp})) - 1$
$f_5 = Y_b^{\text{pred}}(M_Z(\text{exp}))/Y_b(M_Z(\text{exp})) - 1$	$f_6 = Y_\tau^{\text{pred}}(M_Z(\text{exp}))/Y_\tau(M_Z(\text{exp})) - 1$
$f_7 = g_1^{\text{pred}}(M_Z(\text{exp}))/g_1(M_Z(\text{exp})) - 1$	$f_8 = g_2^{\text{pred}}(M_Z(\text{exp}))/g_2(M_Z(\text{exp})) - 1$
$f_9 = g_3^{\text{pred}}(M_Z(\text{exp}))/g_3(M_Z(\text{exp})) - 1$	$f_{10} = v(M_Z(\text{exp}))/v^{\text{pred}}(M_Z(\text{exp})) - 1$
$f_{11} = \tan \beta(M_Z(\text{exp}))/\tan \beta(\text{input}) - 1$	

**Table 2.** Output variables encoding the target boundary conditions. The various quantities are precisely defined in Appendix A. Note that  $f_{11}$  measures how far we are away from a desired input value of  $\tan \beta(\text{input})$ , whereas  $f_2$  measures how far we are away from one of the Higgs potential minimisation conditions, i.e. Eq. (2.7).

in order to satisfy Eq. (3.12), providing a valid solution to the boundary conditions and RGEs (if such a solution exists). We can therefore view the system as 11 simultaneous non-linear equations in the 11  $V_i$ . We solve them by two different methods, depending upon the context: Broyden’s method [20] and a globally convergent Newton-Raphson method, which are both used to find roots of a multi-dimensional function. Here, we shall sketch the Newton-Raphson method that we employ; for more detail on it, or for information about Broyden’s method, see Ref. [19]. We start with some guess for the initial parameters  $V_i$ , and calculate the Jacobian matrix  $J_{ij} = \partial f_i/\partial V_j$  approximately by finite differences.<sup>5</sup>

$$J_{ij} \approx \frac{f_i(V_1, V_2, \dots, V_j + \Delta V_j, V_{j+1}, \dots) - f_i(V_i)}{\Delta V_j} \quad (3.13)$$

for small enough  $\Delta V_j$ . Since

$$f_i(V_j + \Delta V_j) = f_i(V_j) + \sum_j J_{ij} \Delta V_j + \mathcal{O}((\Delta V_j)^2), \quad (3.14)$$

we solve  $\sum_j J_{ij} \Delta V_j = -f_i$  for  $\Delta V_j$ , which solves Eq. (3.14) to leading order for  $f_i(V_j + \Delta V_j) = 0$ . Adding  $\Delta V_j$  onto  $V_j$  should therefore take us closer to a solution of Eq. (3.12). In practice, we require the step to be a *descent direction*, i.e. to first order

$$\frac{1}{2} \sum_j \frac{\partial(\sum_i f_i f_i)}{\partial V_j} \Delta V_j = \sum_{ijk} -f_i J_{ij} J_{jk}^{-1} f_k = -\sum_i f_i f_i < 0. \quad (3.15)$$

If Eq. (3.15) is not satisfied in practice because we are too far from the minimum of  $f_i f_i$  and the second order terms in Eq. (3.14) give a sizeable correction, the algorithm backtracks until we find an acceptable step, as described in more detail in Ref. [19]. These updates are iterated until Eq. (3.12) is satisfied to a given numerical accuracy (specified here to be  $10^{-5}$ ).

Unlike fixed point iteration, the shooting method, implemented using either Broyden or Newton-Raphson for the root finding, does not rely on any restrictions on the size of any

<sup>5</sup>We give here the forward-difference approximation. We have also tried the symmetric-difference approximation, but it runs at almost half the speed due to the additional evaluations of  $f_i$ , and does not give noticeably improved convergence or accuracy.

derivatives in the vicinity of a solution. It is therefore able in principle to find a solution that is unstable to fixed point iteration. For given initial values of the  $V_i$ , one solution (which has some ‘catchment volume’ in  $\{V_i\}$  where the Broyden or Newton-Raphson method will converge to it, see Fig. 12) can be found. The idea then is to run with several randomly chosen  $V_i$  in order to have the possibility of finding the usual fixed-point iteration solutions, the solutions found in Ref. [6] by scanning  $\mu(M_{\text{SUSY}})$ , and any other solutions as well. We have the problem that, for a given number of initial  $V_i$ , we can never guarantee that there are no other solutions other than those we have found. This is a general problem though in any numerical scan, and, failing some analytical breakthrough, there does not appear to be much we can do about it.

## 4 Numerical Procedure

We use a modified version of `SOFTSUSY3.3.6` that implements the shooting method as described above. For a given CMSSM point, first we find a solution using the usual FPI method<sup>6</sup>. We then randomly perturb around this point and run the Broyden or Newton-Raphson root-finding algorithm in order to obtain a solution. The GUT scale parameters  $V_i$  of this solution are checked against those corresponding to any solutions previously found. If any of the  $V_i$  differs by at least 0.001, it is counted as an additional solution and saved. If the  $V_i$  are all within 0.001, we save the solution with the smallest value of  $\max_i |f_i|$ , since this represents the best numerical approximation to solving the boundary conditions. We repeat this procedure 2000 times with different random starting GUT scale initial parameters. It is hoped that 2000 times is sufficient to find all of the solutions, but we can never be sure that this is the case. Our results are usually phrased as scans across the CMSSM parameters, so statistical noise will be seen in any derived plots. Our random perturbations are based on draws from a Gaussian distribution centred on zero of width 1, which we denote  $G_i(1)$  for each independent draw. Each of the  $V_i$  are changed with a probability of 0.5. If perturbed, the  $V_i$  are multiplied in turn by  $|1 + G_i(1) \times a_i|$  (where we must pick values for the real coefficients  $a_i$ ), with the exception of  $V_6 = [m_3^2(M_{\text{GUT}})/10^6 \text{ GeV}^2]$ , which is instead multiplied by  $G_i(1) \times a_6$ .  $V_6$  is singled out for different treatment because we wish to consider either sign for its changed value.

The larger the  $a_i$ , the less likely it is that `SOFTSUSY` will be able to return a physical solution (unphysical solutions could be due to the predicted presence of, for example, tachyons). On the other hand, larger  $a_i$  explores a larger volume of MSSM parameter space within which extra solutions could be found. Choosing all  $a_i$  of order one gives an unacceptably small efficiency, so as to make finding additional solutions extremely unlikely with 2000 ‘shots’. Indeed, trying to find any solution starting from a completely random starting point proved to be impossible: the efficiencies were much too small to find it in 2000 shots.

At tree-level, the  $M_Z$  boundary conditions on the Yukawa and gauge couplings are specified unambiguously by Eqs. (2.1)-(2.4) and experimental data. The quantities  $\mu(M_{\text{SUSY}})$  and  $m_3^2(M_{\text{SUSY}})$  as derived from electroweak symmetry breaking can differ between multiple

---

<sup>6</sup>Sometimes such a solution is not physically viable, but we still use it as a starting point.

solutions, which in turn leads to electroweak one-loop corrections to sparticle threshold corrections to the gauge and Yukawa corrections. Some parameters  $a_i$  correspond to boundary conditions that are fixed at tree-level, but may differ only in electroweak loop corrections. These  $a_i$  we set to have a small value, whereas those  $a_i$  corresponding to boundary conditions that may differ already at tree-level we set to have a larger value. By examining the efficiencies of finding solutions, we find, by trial and error, that the values  $a_i = \{0.03, 0.1, 0.03, 0.03, 1.0, 1.0, 0.03, 0.03, 0.03, 0.03, 0.1\}$  give a reasonably high probability of finding the multiple solutions that we already know about, while retaining an efficiency (defined as the fraction of random perturbations resulting in a physical solution) that is not too small.

The `SOFTSUSY TOLERANCE` parameter fixes how accurately the RGEs are solved.  $\max_i |f_i|$  was also required to be less than `TOLERANCE` within 40 iterations of the Newton-Raphson algorithm (or Broyden’s algorithm). We found that with higher values of `TOLERANCE`, we would obtain higher (and spurious) values of the number of multiple solutions at a CMSSM point: decreasing `TOLERANCE` further meant that some of the apparently different solutions were not good solutions after all, and some of them were actually inaccurately evaluated versions of the same solution. `TOLERANCE` was set to be  $10^{-5}$  for our results below. We have checked for many particular points with multiple solutions that reducing it further did not eliminate any such solutions (reducing `TOLERANCE` further resulted in a higher CPU time cost). We found that the statistical efficiency of our results did depend somewhat on whether we had implemented Broyden’s algorithm, or Newton-Raphson, and furthermore on the precise implementation. Where there was a difference, we used the algorithm which found more multiple solutions, or which displayed less statistical noise in the results.

## 5 Regions of Multiple Solutions

We first provide a map of CMSSM multiple solutions, as determined by the multi-dimensional shooting method outlined above using Broyden’s method. First, we show the results of a scan of  $m_0$  and  $M_{1/2}$  for  $A_0 = 0$  and  $\tan\beta = 40$  (the plane investigated most thoroughly in Ref. [6]). We see that for  $\mu < 0$ , there are two disjoint regions with two solutions in Fig. 2a. In Fig. 2b, we see that for  $\tan\beta = 40, A_0 = 0$  and  $\mu > 0$  that there is a region at high  $m_0$  with multiple solutions near the boundary of successful electroweak symmetry breaking. A line of three multiple solutions exists within this band. Remembering that our method is stochastic in nature, we are not surprised to see that this line is somewhat broken: we expect that, with more statistics, the gaps would be filled in (expecting that the multiple solutions are continuously connected in parameter space). Also, we see that to the top left hand edge of the multiple solution region, there are scattered points. We suspect too that here it is more difficult to find the multiple solutions, and that were we to have more statistics (i.e. run for a higher number of ‘shots’), we would fill in this area. We also see multiple solutions near the electroweak symmetry breaking boundary at high  $m_0$  for  $\mu < 0$  and  $\tan\beta = 10$  in Fig. 2c and for  $\mu > 0$  and  $\tan\beta = 10$  in Fig. 2d. In Fig. 2d, we display the 95% confidence level exclusion contour for ATLAS [21] and CMS [22] searches for events with hard jets and large missing transverse momentum in  $5 \text{ fb}^{-1}$  of  $\sqrt{s} = 7 \text{ TeV}$  LHC data. We see that this exclusion region covers much of the multiple solutions region.

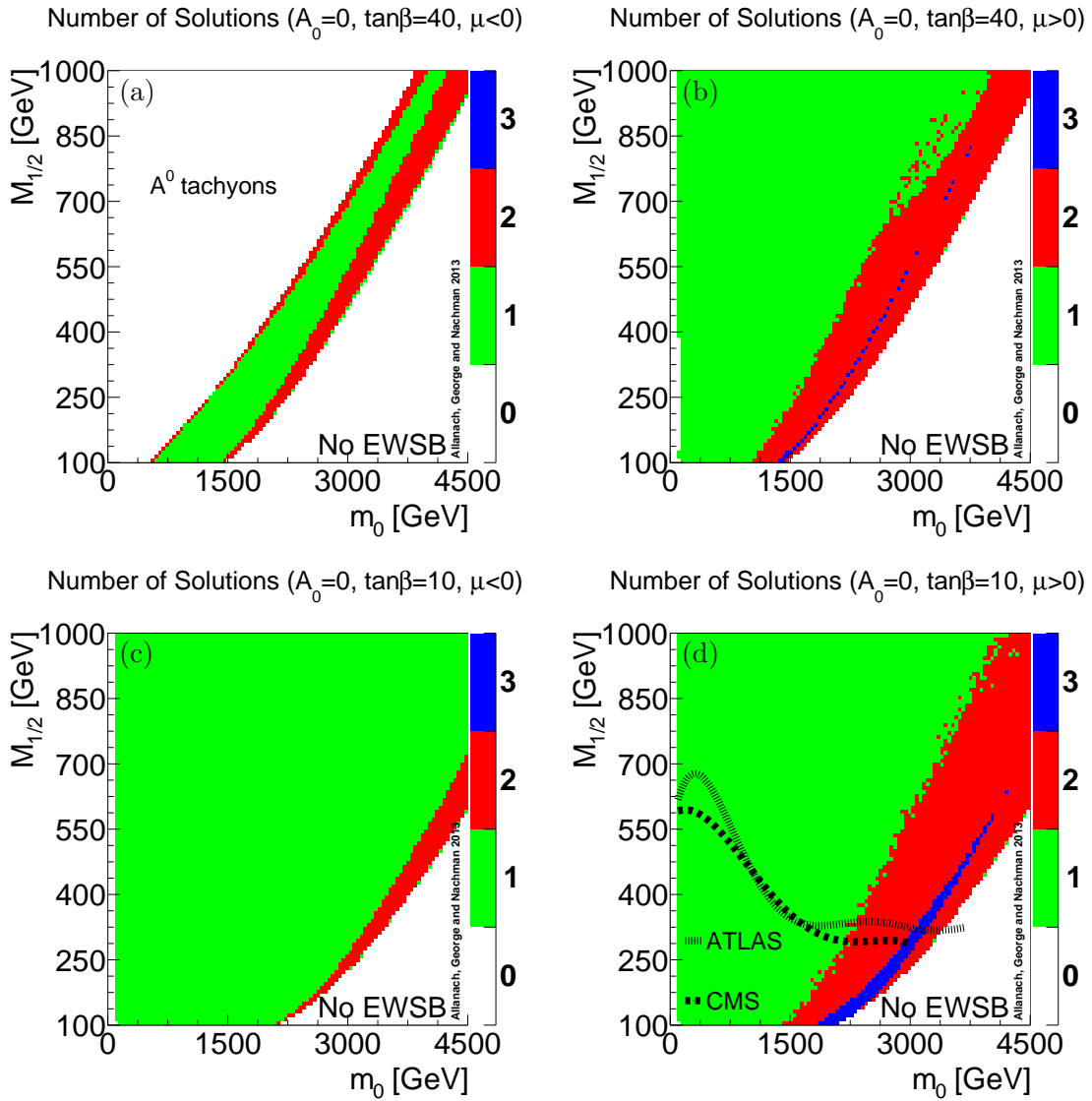


**Figure 2.** Number of solutions in the CMSSM as shown as the background colour and labelled in the key on the right-hand side of each plot for  $A_0 = 0$  and different values of  $\tan\beta$ . White regions have no solutions for the reasons labelled: ‘No EWSB’ denotes a region where there is no acceptable electroweak minimum of the Higgs potential. In (d), the lines display 95% exclusion contours from ATLAS [21] and CMS [22] jets plus missing transverse momentum searches. The region below each contour is excluded.

However, the exclusion region was only calculated using the standard CMSSM solution, so the existence of the additional solutions could potentially affect the bounds. In particular, if mass splittings are significantly different in the new solutions, the acceptance of the cuts would change and so could the corresponding exclusion region. The searches are based on hard jets and missing transverse momentum, and contain lepton vetoes. Thus, if branching ratios of sparticles into leptons were to change significantly between the different solutions, then the predicted SUSY signal event rates would also change, affecting the exclusion regions.

More recent searches by ATLAS, interpreted as exclusions on the CMSSM parameter space have used different parameter planes:  $A_0 = -2m_0$ ,  $\tan\beta = 10$  or  $30$  and  $\mu > 0$  [23]. We have checked these planes for multiple solutions on a 101 by 101 grid, not finding any.

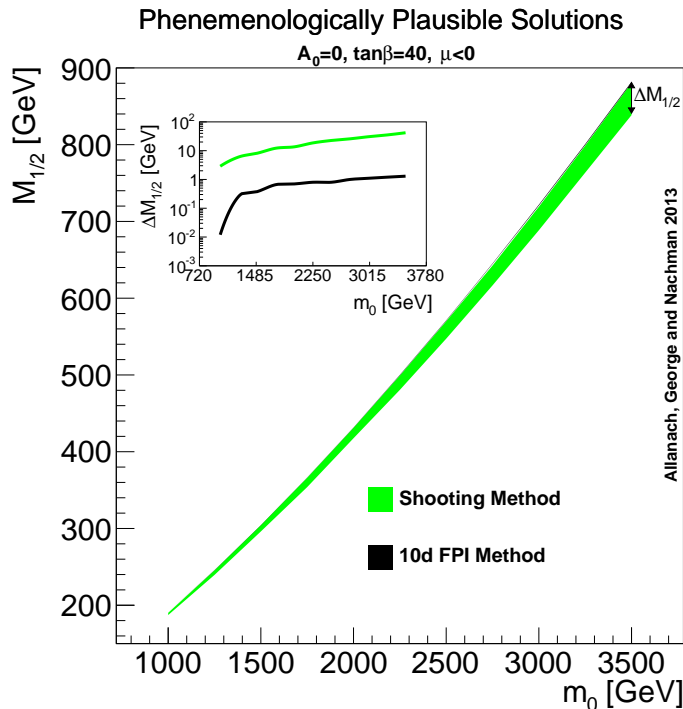


**Figure 3.** A CMSSM extra solution strip for  $A_0 = 0$ ,  $\tan\beta = 40$  and  $\mu < 0$  as computed using a 10d FPI method as in Ref. [6] and the shooting method employed in the present paper. The insert shows the thickness of the strip  $\Delta M_{1/2}$  for various values of  $m_0$ .

Thus, as far as we can tell, exclusion limits derived upon those planes are not compromised by additional solutions.

### 5.1 Comparing algorithms

We now compare our results using the shooting method, to previous estimates in Ref. [6]. There,  $M_Z$  was predicted by initially relaxing the boundary condition Eq. (2.6), scanning in one dimension,  $\mu(M_{\text{SUSY}})$ , and using fixed point iteration in the remaining 10 dimensional parameter space per CMSSM point. Luckily, the existence of additional solutions was demonstrated, but in fact many of them could have been missed due to the fact that FPI was still being used, which could have the concomitant stability issues sketched in Sec. 3.1. In fact, the solutions found with the shooting method are a superset of those found in Ref. [6].

Comparing the results in Fig. 2 to equivalent estimates in Ref. [6] using the different methodology, we see some differences: we now find a much larger area of the parameter plane with multiple solutions. For example, we compare maps of a particular strip with two solutions in Fig. 3. We shall show below that this strip is of particular interest because it predicts sparticle masses that are not already excluded by LEP2. The new determination of this multiple solution region using the multi-dimensional shooting method is shown in green on the figure, whereas the one-dimensional method of Ref. [6] only finds the region

in the black line. The insert shows that the width of the strip as measured by  $M_{1/2}$  (for a given  $m_0$ ) increases by a factor of several tens, providing a quantification of how much better the shooting method performs.

It is hard to compare the speed of the FPI computation versus that of our implementation of the shooting method, because often the shooting method will not find a solution. FPI also does not find additional solutions, and returns ‘no-convergence’ errors near the boundary of electroweak symmetry breaking. On the other hand when the shooting method works, the solution is typically much more accurate (i.e.  $M_Z^{\text{pred}}/M_Z^{\text{exp}}$  is typically much closer to 1). However, given these caveats, it is still probably helpful to give some idea of the relative speeds. In the case where FPI finds the same solution as our implementation of the shooting method, FPI is quicker. The vast majority of the run-time is taken up with running the RGEs between  $M_{\text{GUT}}$  and  $M_Z$ . Thus, we may use this as an approximate unit of time taken for the program to run. For each iteration of the shooting method we need to run the RGEs from  $M_{\text{GUT}}$  to  $M_Z$  12 times (one for the central value, and 11 to determine the 11 forward derivatives in the Jacobian). This needs to be repeated typically a few times to converge on a solution (if indeed it does converge). FPI on the other hand, takes around 3-10 iterations, depending upon the parameter point<sup>7</sup>. Each of these iterations consists of running from  $M_{\text{GUT}}$  to  $M_Z$  and then back again, i.e. two time units. These rough estimates tell us that the shooting method is expected to be a few units slower than the FPI method when it achieves a solution. This is often increased by a factor of 2-10 because the shooting method takes that number of shots before a viable solution is found.

To get a quantitative understanding of the difference in speed of the algorithms, we performed rectangular scans over part of Fig. 6a for three algorithms: 1) pure FPI, 2) FPI to obtain a starting point, perturbing randomly around this point, then shooting with Newton-Raphson and a forward derivative, and 3) same as 2) but with a symmetric derivative (twice as many evaluations of the RGEs). We have  $\tan \beta = 10$ ,  $A_0 = 0$  and look for positive  $\mu$  solutions. Scanning with a  $31 \times 31$  grid over the range  $m_0 = 1500 - 3000$  GeV and  $M_{1/2} = 500 - 800$  GeV algorithms 1, 2 and 3 took 126, 437 and 701 seconds respectively. Compared with pure FPI, the shooting method will always take longer because it does all the computations of FPI (to find the initial guess), plus additional computation for Newton-Raphson convergence. It is thus best to summarise the running times as: the shooting method with forward derivatives added 247% to the running time of normal FPI, and with symmetric derivatives, 456%. The latter number is not quite twice the former (as naïvely expected) since, for example, the Newton-Raphson matrix inversion does not have to be repeated twice when going from forward to symmetric derivatives.

Because convergence properties differ over the CMSSM parameter space, we also scanned a rectangular grid that included part of the no-EWSB region. We ran a  $31 \times 21$  grid over the range  $m_0 = 3000 - 4500$  GeV and  $M_{1/2} = 400 - 600$  GeV (with all other parameters the same as in the previous scan). Per point, this region ran slower than the previous region. Algorithms 1, 2 and 3 took 230, 603 and 946 seconds respectively. Compared with

---

<sup>7</sup>However, points close to the boundary of electroweak symmetry breaking can take up to 100 iterations, or indeed never converge.



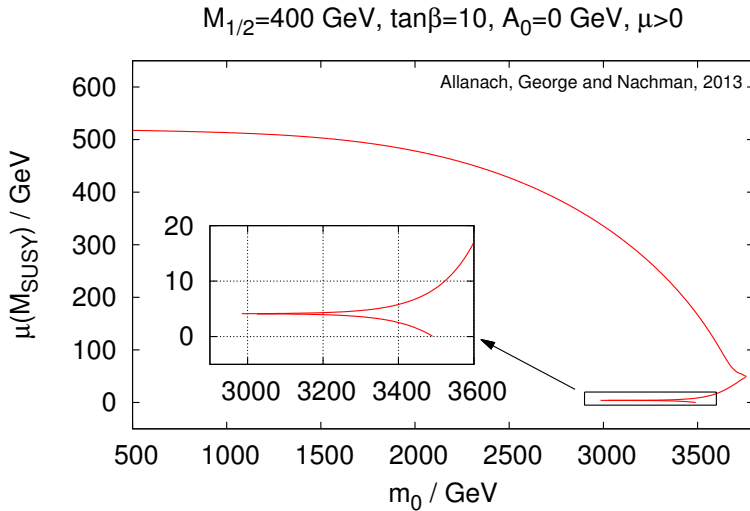


**Figure 4.** A scan over  $m_0$  in the CMSSM, solving all 11 low-scale constraints, and plotting the value of  $\mu(M_{\text{SUSY}})$  for all the solutions. It is clear that the values for  $\mu(M_{\text{SUSY}})$  can differ greatly among the multiple solutions. For values of  $m_0$  larger than those shown, electroweak symmetry is not successfully broken.

pure FPI, these numbers correspond to an additional 162% and 311% for the forward and symmetric derivative shooting methods, respectively.

## 5.2 The LEP2 limit

We shall see that a sparticle mass bound derived at LEP2 in the context of the CMSSM imposes strong constraints upon the additional solutions. The 95% CL lower limit on the chargino mass from LEP2 is 102.5 GeV [24] within CMSSM-like models.

The Lagrangian contains the chargino mass matrix  $-\tilde{\psi}^{-T} \mathcal{M}_{\tilde{\psi}^+} \tilde{\psi}^+ + h.c.$ , where  $\tilde{\psi}^+ = (-i\tilde{w}^+, \tilde{h}_2^+)^T$ ,  $\tilde{\psi}^- = (-i\tilde{w}^-, \tilde{h}_1^-)^T$ ,  $\tilde{w}^\pm = (\tilde{w}^1 \mp i\tilde{w}^2)/\sqrt{2}$  for the charged winos and  $\tilde{h}_1^-, \tilde{h}_2^+$  for the charged higgsinos. We also have, at tree level,

$$\mathcal{M}_{\tilde{\psi}^+} = \begin{pmatrix} M_2 & \sqrt{2} M_W s_\beta \\ \sqrt{2} M_W c_\beta & \mu \end{pmatrix}. \quad (5.1)$$

The chargino masses correspond to the singular values of  $\mathcal{M}_{\tilde{\psi}^+}$ , i.e. the positive square roots of the eigenvalues of  $\mathcal{M}_{\tilde{\psi}^+}^\dagger \mathcal{M}_{\tilde{\psi}^+}$  [25]:

$$M_{\chi_{1,2}^\pm}^2 = \frac{1}{2} \left\{ \mu^2 + M_2^2 + 2M_W^2 \mp [(\mu^2 + M_2^2 + 2M_W^2)^2 - 4\mu^2 M_2^2 - 4M_W^4 \sin^2 2\beta + 8M_W^2 \mu M_2 \sin 2\beta]^{1/2} \right\}. \quad (5.2)$$

This places a strong constraint on many of our multiple solutions, whose values of  $\mu$  differ (and therefore the lightest chargino mass computed by Eq. (5.2) differs). In Fig. 4 we

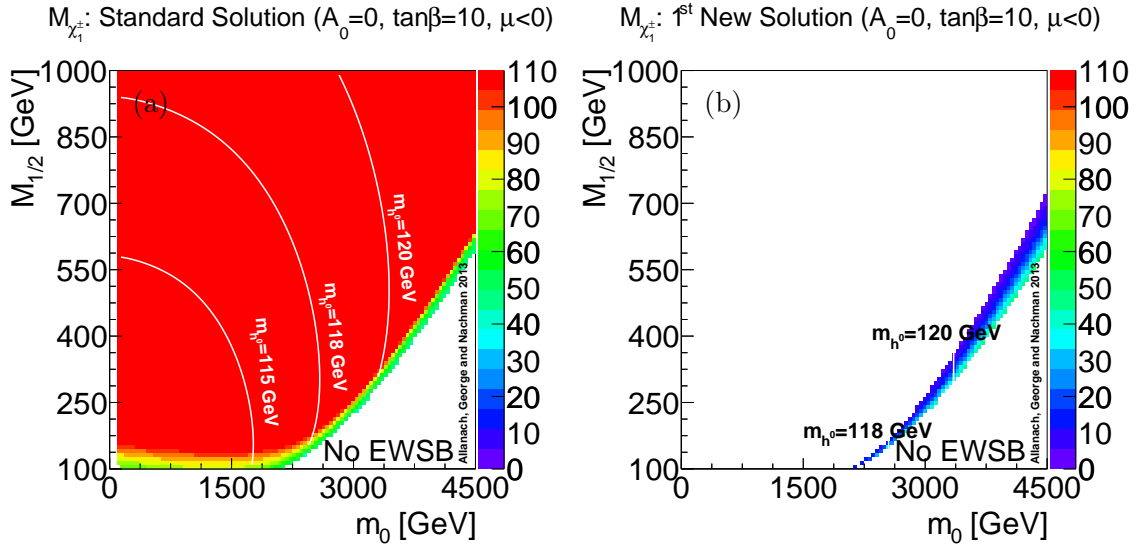


**Figure 5.** Lightest chargino mass in the CMSSM for  $A_0 = 0$ ,  $\tan\beta = 10$  and  $\mu < 0$ . White contours are iso-contours of lightest CP-even Higgs mass  $m_{h^0}$ . The additional solutions in (b) are ruled out by the LEP2 lower limit on the chargino mass of 102.5 GeV.

show the behaviour of  $\mu(M_{\text{SUSY}})$  for all the solutions that can be found as  $m_0$  changes, for  $M_{1/2} = 400$  GeV,  $A_0 = 0$ ,  $\tan\beta = 10$  and  $\mu > 0$  (for this plot we used Newton-Raphson). For high enough  $m_0$ , electroweak symmetry breaking no longer works and so we no longer have any solutions to plot (i.e. for  $m_0 > 3.76$  TeV). The appearance of additional solutions near the electroweak symmetry breaking boundary was qualitatively explained in Ref. [6]. To summarise, the RGE corrections which change  $\mu$  have a larger than usual effect in this region because  $\mu$  approaches zero at the boundary. In the figure, we see how  $\mu(M_{\text{SUSY}})$ , derived from minimising the Higgs potential, starts at a high value at moderate  $m_0$ , and decreases as  $m_0$  is increased and as the boundary of successful symmetry breaking is approached. This is fairly generic behaviour, and applies for different values of  $M_{1/2}$ . For  $m_0 \in [3 \text{ TeV}, 3.5 \text{ TeV}]$ , we obtain two additional solutions. Between the different solutions, we observe very different values of  $\mu(M_{\text{SUSY}})$ . The additional solutions have rather low values (again, generic behaviour near the boundary of electroweak symmetry breaking), predicting a low  $M_{\chi_1^\pm}$  once loop corrections have been added to Eq. (5.2).

In particular, the multiple solutions near the boundary of electroweak symmetry breaking have a smaller value of  $\mu(M_{\text{SUSY}})$  than the standard solution, with a consequently smaller chargino mass. We plot the chargino mass as the background colour of Figs. 5, 6, 7 and 8 for the standard solutions and the new solutions found by our shooting algorithm using Broyden's method. We see from Figs. 5a, 6a that, for the standard solutions, only a small region right next to the EWSB boundary has  $M_{\chi_1^\pm} < 102.5$  GeV, and falls afoul of the LEP2 chargino mass constraint for  $\tan\beta = 10$  and either sign of  $\mu$ . Figs. 5b, 6b and 6c show that the multiple solutions all *fail* the LEP2 chargino mass constraint for  $\tan\beta = 10$  and  $A_0 = 0$ . Once this is taken into account, the additional solutions do not resurrect any

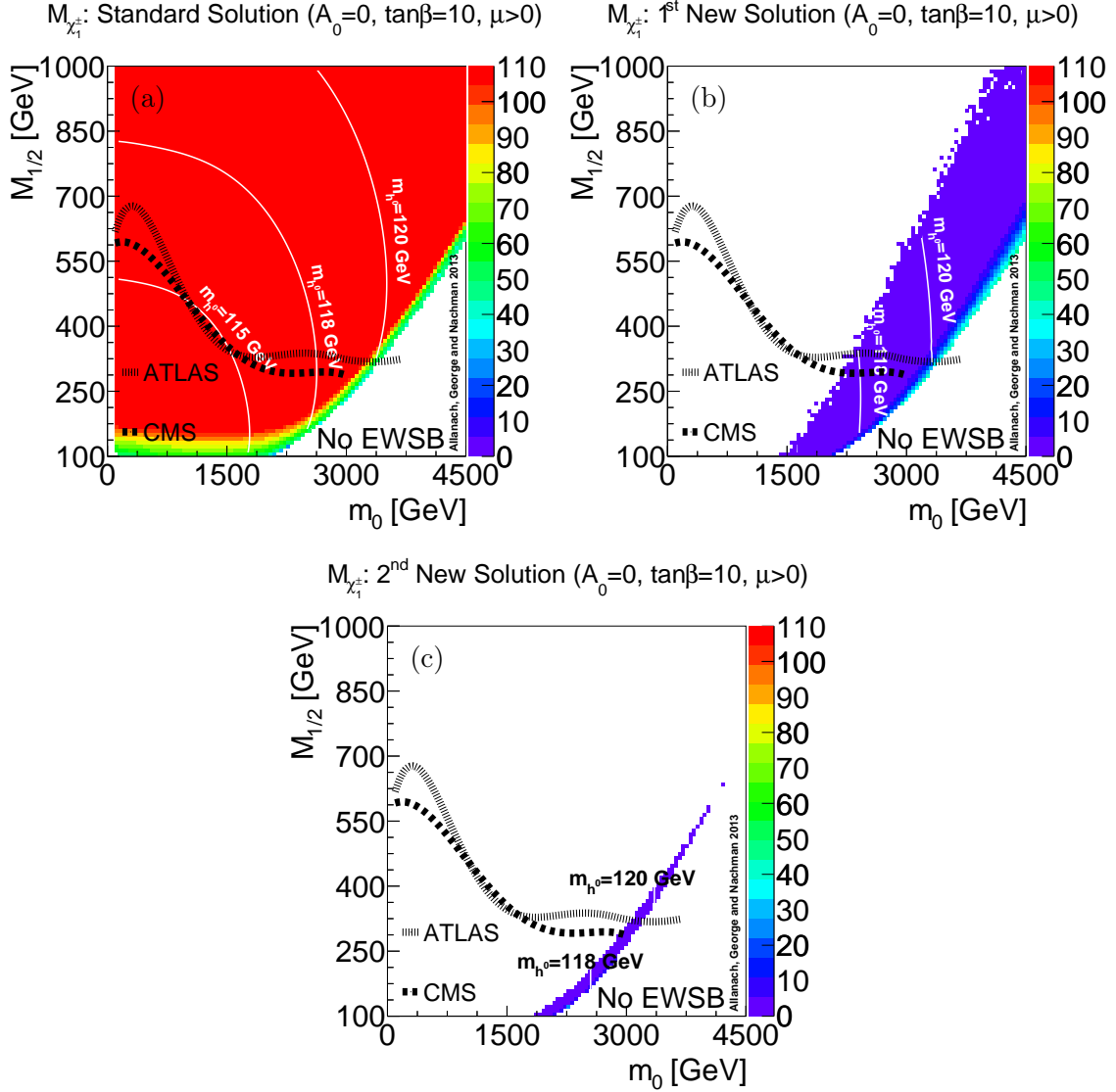


**Figure 6.** Lightest chargino mass in the CMSSM for  $A_0 = 0$ ,  $\tan\beta = 10$  and  $\mu > 0$ . White contours are iso-contours of lightest CP-even Higgs mass  $m_{h^0}$ . The additional solutions in (b) and (c) are all ruled out by the LEP2 lower limit on the chargino mass of 102.5 GeV.

points that were already ruled out by the 95% CL region of ATLAS and CMS, as shown in Fig. 6, for example. The LHC limits are therefore unchanged on the  $\tan\beta = 10, \mu > 0$  plane.

More generally, from Figs. 5, 6, 7 and 8 we see that every additional solution in the class adjacent to the no EWSB region *fails* the LEP2 chargino mass constraint for  $A_0 = 0$ ,  $\tan\beta = 10$  and  $\tan\beta = 40$  and either sign of  $\mu$ . This means that the only viable additional solution strip shown in these plots is the one at higher values of  $M_{1/2}$  in Fig. 7b. We refer to this as the “phenomenologically plausible strip”.

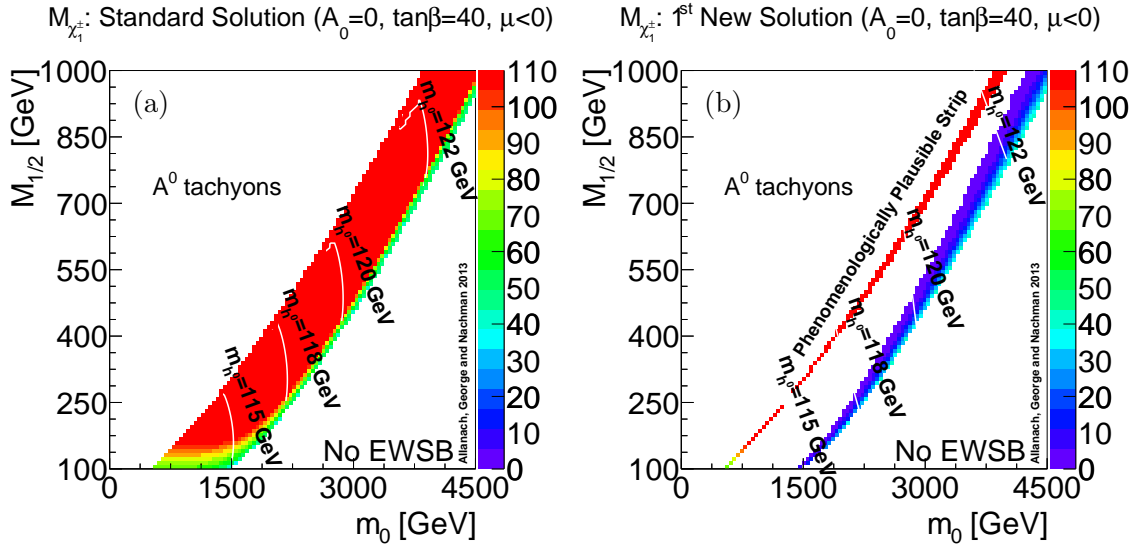


**Figure 7.** Lightest Chargino mass in the CMSSM for  $A_0 = 0$ ,  $\tan\beta = 40$  and  $\mu < 0$ . White contours are iso-contours of lightest CP-even Higgs mass  $m_{h^0}$ . (b) has a strip of phenomenologically plausible solutions.

We also show iso-contours of the lightest CP even Higgs mass in Figs. 5, 6, 7 and 8. One should bear in mind an estimated 3 GeV error upon the prediction coming from higher order corrections. Much of the available parameter space is ruled out by the recent LHC measurements of a boson consistent with a 125 GeV Higgs [26, 27]. While this bound is not the main focus of the present paper, we see from Fig. 7b that there is an allowed region with multiple solutions: the phenomenologically plausible strip with  $m_{h^0} > 122$  GeV.

### 5.3 The phenomenologically plausible strip

The only region of parameter space investigated that has additional solutions which are not excluded outright by the LEP2 chargino bounds is the thin phenomenologically plausible strip (the upper region in Fig. 7b, also shown in Fig. 3). In this region, the  $\overline{DR}$  CP-odd neutral Higgs mass  $m_{A^0}$  tends toward zero, enhancing its loop correction in threshold effects (for example to Yukawa and gauge couplings). This enhancement allows for larger than usual corrections, leading to the presence of multiple solutions. For more detail see Ref. [6]. We shall now study the phenomenological properties of solutions along this strip in more depth. In particular, we wish to know how much the sparticle masses and other observables differ between the different solutions. If sparticle masses differ by less than 1% or so, then the solutions are similar enough such that LHC exclusion regions are unlikely to be different for the separate solutions. However, if there are significant differences in masses leading to different kinematics of SUSY signal events, cut efficiencies may be different enough to alter exclusion regions. We should bear in mind, however, that a future linear collider could be sensitive to fractional mass differences even at the sub-percent level, particularly in the slepton/chargino/neutralino sectors [28]. Thus, even sub-percent differences could be

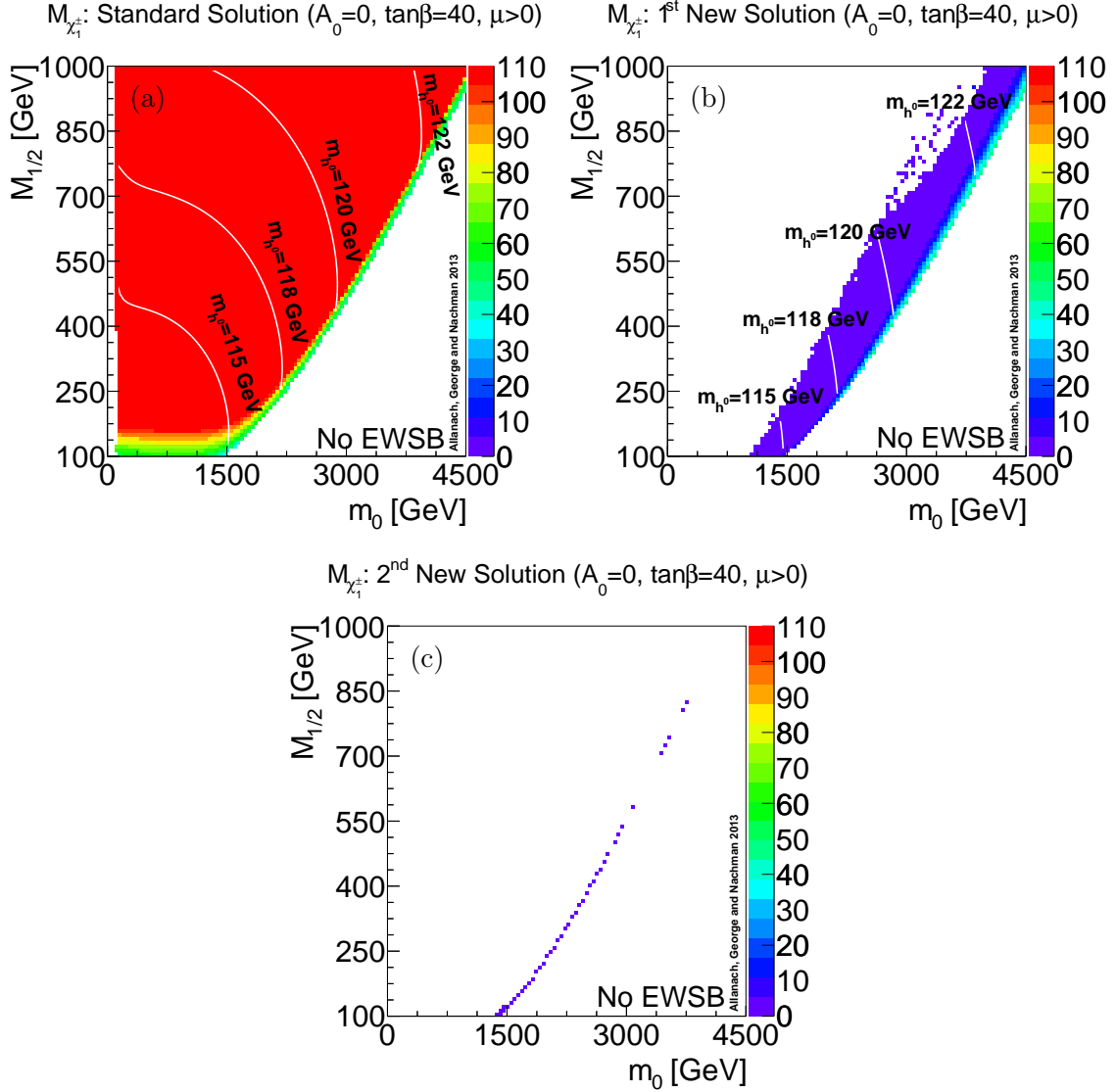


**Figure 8.** Lightest Chargino mass in the CMSSM for  $A_0 = 0$ ,  $\tan\beta = 40$  and  $\mu > 0$ . White contours are iso-contours of lightest CP-even Higgs mass  $m_{h^0}$ . The additional solutions in (b) and (c) are all ruled out by LEP2.

relevant for future searches or measurements. The branching ratios of sparticle decays may also be affected by changes in masses and MSSM couplings. These may then in turn affect event rates for the production of particular final states. It was already shown in Ref. [6] that the values of  $\mu(M_{\text{SUSY}})$  and  $m_3^2(M_{\text{SUSY}})$  vary more than other parameters between the different solutions. The masses of MSSM particles that are most sensitive to  $\mu(M_{\text{SUSY}})$  and  $m_3^2(M_{\text{SUSY}})$  are: neutralino<sup>8</sup> and chargino masses, third generation sparticle masses

<sup>8</sup>It is the higgsino mass that depends upon  $\mu(M_{\text{SUSY}})$ , and so only those neutralinos that have a significant higgsino component will show a significant sensitivity. Near the boundary of bad electroweak symmetry

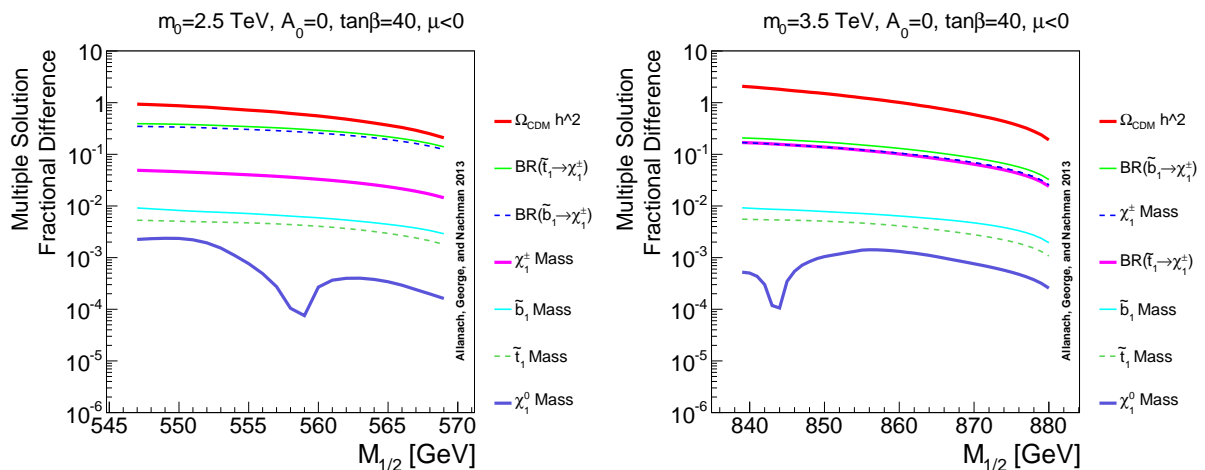


**Figure 9.** Fractional differences between the multiple solutions for various phenomenological properties at two slices of the phenomenologically plausible strip. The ordering in the legend matches the ordering of the plotted lines.

and the pseudo-scalar Higgs boson mass. We shall display some of these differences below. We shall also display branching ratios of stop and sbottom decays into charginos because they illustrate some significant differences between the two solutions.

Fig. 9 shows how the fractional difference between the multiple solutions for various phenomenological properties varies across the strip for two fixed values of  $m_0$ . The MSSM spectrum and coupling information was passed with the SUSY Les Houches Accord format [29] to SUSY-HIT [30], which calculated the branching ratios. Dark matter properties were then computed using micrOMEGAs [31, 32]. For a given calculated phenomenological parameter  $X$ , the fractional difference is defined as  $|X_1 - X_2|/X_1$  where  $X_1$  is the predicted value of  $X$  corresponding to the solution with a higher chargino mass and  $X_2$  corresponds to the solution with the lower chargino mass. While there are only sub-percent level differences between the masses of the lightest third-generation squarks and the lightest neutralinos, there are significant deviations for other quantities. The most significant differences are in the predicted thermal relic density of neutralino cold dark matter,  $\Omega_{\text{CDM}} h^2$ , in which there can be 100% differences, depending upon the universal model parameters. There are also large differences at the tens-of-percent level in the branching ratio of the third generation squarks into charginos. At high  $m_0$ , the chargino mass itself can also vary at the 10% level, which would necessarily affect the limits placed on this region of parameter space for analyses employing charginos in decays [33]. At lower values of  $m_0$ ,  $M_{\chi_1^\pm}$  differs only at the percent level and so we would not expect there to be a large impact on limits. Thus, even though the chargino mass is large enough along the strip for the solutions to be viable, for a portion of this strip the phenomenological properties are so close that excluding one solution would also result in excluding the additional solution.

---

breaking at high  $m_0$ , there is sensitivity in the lightest neutralino mass, but for lower  $m_0$ , only the heavier neutralinos show any mass changes.

## 5.4 Example of Dark Matter Differences

Now we exemplify the most important difference between the solutions: that of a different predicted thermal relic density of dark matter in the universe. Recently, data from the Planck satellite have been used to derive the constraint [34]

$$\Omega_{CDM}h^2 = 0.1198 \pm 0.0026. \quad (5.3)$$

We place a dominant theoretical uncertainty on our prediction of 0.01 coming from loops (the thermal relic density is only calculated by `micrOMEGAs` to tree-level order), and therefore require the predicted thermal relic density of neutralinos to be  $\Omega_{CDM}h^2 \in [0.0998, 0.1398]$ . After a brief scan, we found a parameter point in the phenomenologically plausible strip ( $m_0 = 760$  GeV,  $M_{1/2} = 141.72$  GeV,  $A_0 = 0$ ,  $\tan\beta = 40$ ,  $\mu < 0$ ) where the standard solution predicts  $\Omega_{CDM}h^2 = 0.34$ , i.e. well outside of this range, but where the *additional* solution prediction of  $\Omega_{CDM}h^2 = 0.118$  is near the central value. It turns out that this point has the  $\chi_1^0$  mass being approximately half of the Higgs mass. The  $\chi_1^0$  mass, which changes slightly between the solutions, is more exactly half the lightest CP even Higgs mass for the additional solution, which leads to very efficient annihilation of neutralinos through an  $s$ -channel  $h^0$  into quark or lepton pairs, significantly reducing the relic density from 0.34 to 0.118.

## 5.5 Explorations in parameter space

It is possible to relax one or more of the constraints  $f_i$  at the low scale and solve only a subset of these equations. Doing so will highlight the existence of multiple solutions, and give insight into how much the low-scale predictions change with respect to input parameters. For each constraint that is relaxed, there will be one high-scale parameter  $V_j$  (it doesn't matter which one) that is no longer determined by the Newton-Raphson solver. Such high-scale parameter(s) are controlling parameters, in that we now fix them for the solution of that point. To get a feeling for how the parameter space looks we can scan these parameters — fix them at successive values — and plot the resulting function  $f_i$  which has been left unconstrained.

Here, we choose to relax the  $M_Z(\text{pred})^2$  constraint (i.e.  $f_1$  can take any value) and the single controlling high-scale parameter is  $V_5 = [\mu(M_{\text{GUT}})/1000 \text{ GeV}]^2$ . We scan  $V_5$  over a large range and use the Newton-Raphson method to solve for the remaining 10 parameters using the remaining 10 constraints. Because the parameter space is large, we utilise a “line walking” technique in order to improve the efficiency of finding solutions for a given  $V_5$ . Given two solutions that satisfy the 10 low-scale constraints, and are close in  $V_5$  at the high-scale, we can use a linear approximation on the  $V_i$  to project and make a guess at the high-scale parameters for the solutions either side of these original 2. Doing this successively allows us to “walk” through the high-scale parameter space, using  $V_5$  as the parameter of the line, finding adjacent points that satisfy the 10 low-scale constraints. The initial point used is the one found by the standard FPI method.

The output of this line walking is a list of points in the 11-dimensional high-scale parameter space, one point for each value of  $V_5$ . These points represent a function ( $f_1 =$



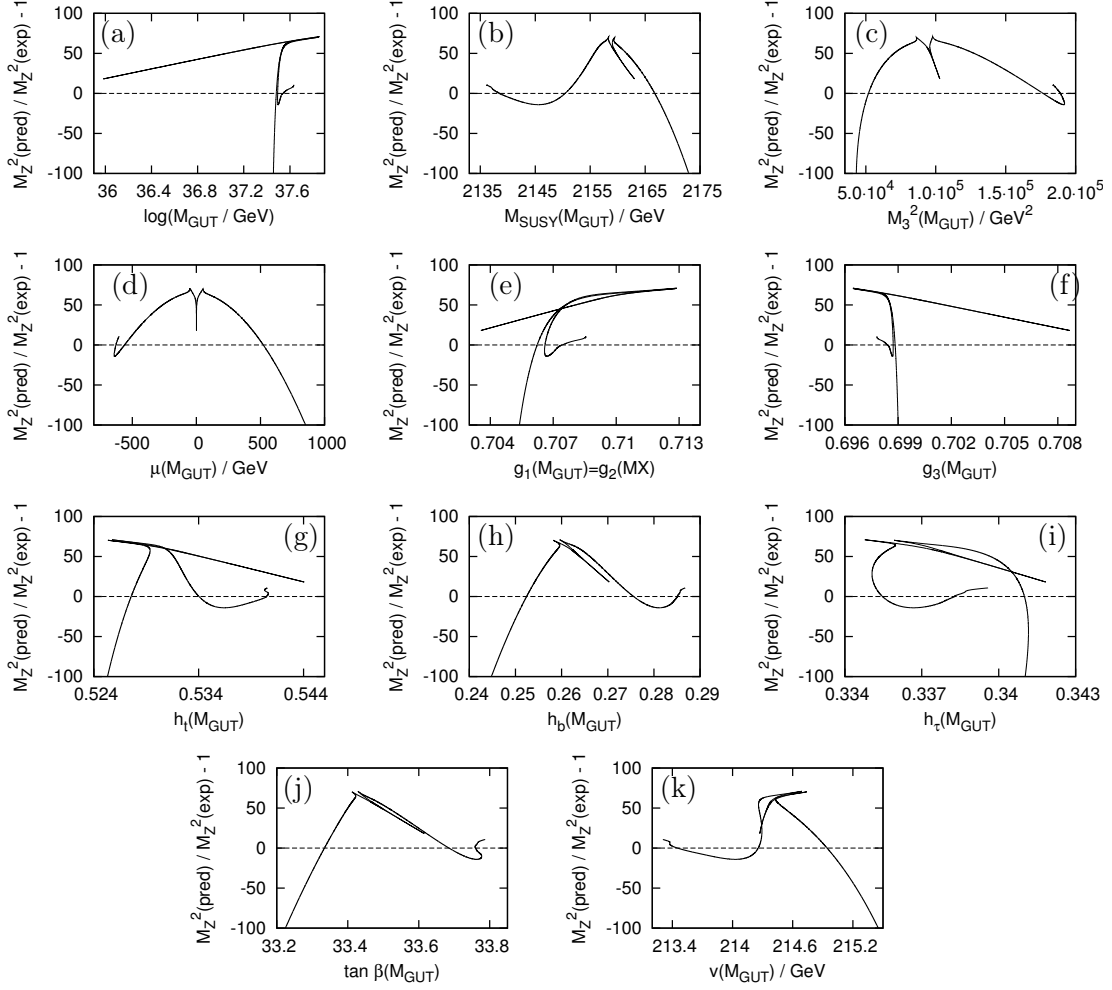


**Figure 10.** The 11 projections of a function defined on the 11-dimensional high-scale parameter space, determined by relaxing the  $M_Z$  low-scale constraint  $f_1 = M_Z(\text{pred})^2/M_Z(\text{exp})^2 - 1$ . Where the solid line crosses the horizontal dashed line, the predicted value of  $M_Z$  matches the experimental value ( $f_1 = 0$ ) and we have a solution which satisfies all 11 low-scale constraints. We used  $\tan \beta = 40$ ,  $A_0 = 0$  GeV,  $m_0 = 2855$  GeV,  $M_{1/2} = 660$  GeV.

$M_Z(\text{pred})^2/M_Z(\text{exp})^2 - 1$  defined on the high-scale parameter space, and we plot all 11 projections of  $f_1$  in Fig. 10, for both signs of  $\mu$  (as illustrated by Fig. 10d<sup>9</sup>). Points where the function  $f_1$  crosses 0 correspond to full solutions of all boundary conditions and RGEs. Fig. 10d shows that, for this CMSSM point, there are two solutions for  $\mu < 0$  and one for  $\mu > 0$ . These three solutions are evident in each of the other ten projections, although sometimes they are very close and hard to spot (for example in Fig. 10a). Each individual projection is non-smooth, and none of the one dimensional projections yield a uniquely defined function (i.e. for some values of each abscissa coordinate, there is more than

<sup>9</sup>Note that the sign of  $\mu$  is an RGE invariant, therefore the  $\text{sgn}(\mu(M_{\text{GUT}})) = \text{sgn}(\mu(M_{\text{SUSY}}))$ .

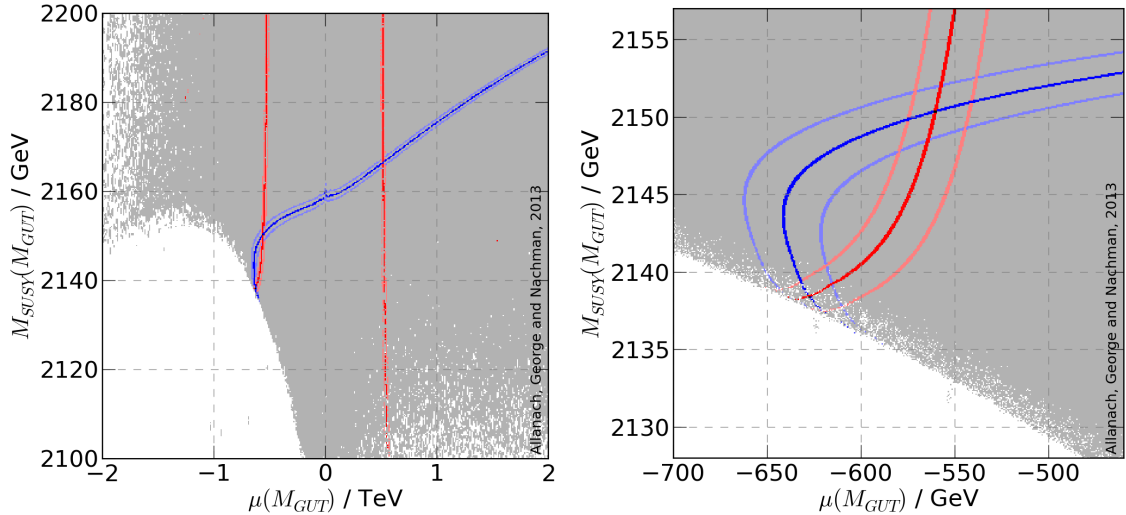


**Figure 11.** Exploration of parameter space found by relaxing  $f_1$  and  $f_{11}$  in the CMSSM with for  $\tan\beta = 40$ ,  $A_0 = 0$  GeV,  $m_0 = 2855$  GeV and  $M_{1/2} = 660$  GeV. On the left we show a larger domain, but on the right we show a zoomed in domain of the  $\mu < 0$  region including two solutions of the full system. On the centre red contour line,  $M_Z^2$  is correctly predicted, on the centre blue contour,  $\tan\beta(M_Z(\text{exp}))$  is. Where these contours intersect, all 11 constraints are satisfied; this occurs 3 times. The additional red contours on either side of the centre contour show where the error  $f_1 = M_Z(\text{pred})^2/M_Z(\text{exp})^2 - 1$  is  $+4$  and  $-3$ , i.e. the predicted  $Z$  mass is 2 times the experimental one, physical or tachyonic, respectively. For the additional blue contours  $f_{11}$  is  $\pm 5 \times 10^{-3}$ , i.e.  $\tan\beta(M_Z(\text{exp}))$  is 0.5% higher or lower than the input value, as per Eq. (2.1). The white region has tachyonic  $A^0$ s and does not yield physical solutions.

one predicted  $f_1$  value). The non-smoothness yields practical difficulties when solving the system: the Newton-Raphson solver uses derivatives and the finite difference approximation to them becomes huge in the vicinity of a non-smooth piece. This can send the solver off to extreme and unphysical parts of parameter space, where we cannot obtain sensible solutions of the RGEs (for example, because of poles in renormalising quantities, or because tachyons are predicted). In this case, the attempt in question must be abandoned, and another started with a different random starting point. If that starting point is on the correct side of the kink, such that it can reach a full solution without encountering the kink again, then a solution may be found. This illustrates one of the reasons for requiring a stochastic approach where we fire many different shots in order to find the different solutions. To summarise: non-smoothness sometimes provide difficulties for the Newton-Raphson solver, whereas (as explained in Section 3.1), the magnitude of the derivatives at the horizontal zero line affects the stability of the FPI algorithm.

In a separate study we then relaxed two constraints:  $M_Z(\text{pred})^2$  and  $\tan\beta(M_Z(\text{exp}))$ , equivalently  $f_1$  and  $f_{11}$ . We computed  $f_1$  and  $f_{11}$  over the two-dimensional plane of our freed-up parameters, chosen here to be  $M_{\text{SUSY}}(M_{\text{GUT}})$  and  $\mu(M_{\text{GUT}})$ , controlled by  $V_{11}$  and  $V_5$  respectively. Within a rectangular region in this plane we pick random initial points and attempt to obtain a solution to the 9 low-scale constraints (we vary the density of

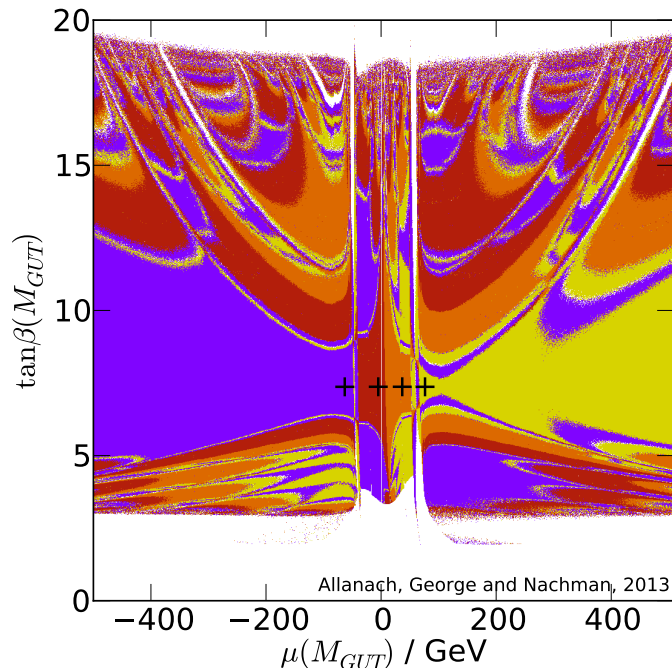


**Figure 12.** Exploration of the high-scale parameter space to find the ‘catchment volume’ of the Newton-Raphson solver in the  $(\mu, \tan \beta)$  plane. Each point in the figure denotes a specific starting point for the high-scale parameters, and the colour of the point tells which solution the solver converges on. There are 4 different solutions. The values of  $\mu$  and  $\tan \beta$  for the converged solutions are shown by the black plus-symbols. White indicates that the solver could not converge with the corresponding initial high-scale parameters. We used  $\tan \beta = 10$ ,  $A_0 = 0$  GeV,  $m_0 = 2800$  GeV,  $M_{1/2} = 200$  GeV.

points near the full solutions to provide more clarity). These functions each have contours at zero which predict the correct value for a low-scale constraint, in direct analogy with the lines in Fig. 10 passing through zero. Where these contours from the two unconstrained  $f$ ’s intersect, we have a complete solution satisfying all 11 constraints. This is shown in Fig. 11. The standard solution for  $\mu < 0$  is at higher values of  $M_{\text{SUSY}}(M_{\text{GUT}})$ . We can see from the figure that the additional solution here is close to the physical boundary, where the  $A^0$  becomes tachyonic (shown as the white region in the plots). We also see from the figure that  $\tan \beta(M_Z(\text{exp}))$  varies much more slowly across parameter space than  $M_Z(\text{pred})^2$ . The figure also illustrates how difficult it is in general to obtain a solution: there is a large volume of unphysical (white) parameter space, and indeed the outer side of the red contours the  $Z^0$  is tachyonic, yielding unphysical parameter space. The problem is much exacerbated in the full 11-dimensional case, rather than just this two-dimensional scan.

We also studied the behaviour of the Newton-Raphson solver by determining the ‘catchment volumes’ of the various solutions for one particular point in CMSSM parameter space. Figure 12 shows the result. We first find a solution using the FPI algorithm, and use this

to fix 9 of the high-scale parameters. The other 2, being  $\mu(M_{\text{GUT}})$  and  $\tan\beta(M_{\text{GUT}})$ , are scanned across a grid, as per the axis of the figure. Each point then corresponds to a distinct point in the high-scale parameter space, and we then use it as the *initial* guess for the Newton-Raphson solver. We then run the solver until it converges (or not) on a solution. If it converges, we colour the point depending on which solution it finds. In this example there are 4 different solutions, 2 with  $\mu < 0$  and 2 with  $\mu > 0$ . The results are very sensitive to the particulars of the solver (such as tolerance, and criteria for convergence), but they serve to illustrate the fact that there are many sharp and non-trivial features in the equations that any solver must deal with.

## 6 Summary and conclusions

We have provided a method to search in an efficient, multi-dimensional way for multiple solutions to RGEs. The methodology that we employ should work in general for theories which have multiple renormalising quantities, with boundary conditions placed upon them at different renormalisation scales. It dispenses with fixed point iteration (the algorithm used by publicly available spectrum calculators), which can have stability problems for some of the solutions, and uses the shooting method instead. One shoots at low-scale boundary conditions only in one direction, by first imposing high scale boundary conditions and then running the RGEs down. Standard methods to solve non-linear simultaneous equations are then used —in this paper both Broyden’s method and Newton-Raphson — to find solutions to the low-scale boundary conditions. To find several solutions, several shots are taken, each with random starting values of the high-scale parameters consistent with the high-scale boundary conditions. One problem that will be present in any such numerical scan is that one can never be completely sure that one has found all of the solutions, unless something analytically can be said about their number.

In a previous work [6] it was shown that the CMSSM has multiple solutions in some parts of its parameter space. The multiple solutions are characterised by the fact that they have the same  $m_0$ ,  $M_{1/2}$ ,  $A_0$ ,  $\tan\beta$  and  $\text{sgn}(\mu)$ , yet are physically distinct, with different sparticle masses and couplings. The existence of multiple solutions was demonstrated by inverting one of the boundary conditions and using fixed point iteration in the other 10 dimensions of parameter space. Some solutions may be unstable to fixed point iteration, however, which means that such an algorithm will never find them. The shooting method has no such stability issues (that we are aware of), and can in principle find all of the solutions. This is done by randomly perturbing an initial guess of high-scale parameters consistent with the high-scale boundary conditions, then homing in on a solution with a non-linear multi-dimensional simultaneous equation solver. One repeats this several times, hoping with each ‘shot’ to find a different solution. Given enough shots, the method can find all of the solutions. However, for a finite number of shots, one can never guarantee that one has found all of them. In the present paper, we have shown that using the shooting method instead of fixed point iteration not only finds the previously discovered additional solutions, but also finds new ones too. It was also our intention here to study the multiple solutions phenomenologically, to see whether they are ruled out by experimental data, and

to see to which extent they differ from the standard solutions (and if, for example, LHC searches need to be reinterpreted taking the multiple solutions into account).

We find that CMSSM multiple solutions come in two classes. One class, at extreme values of large  $m_0$  just under the no electroweak symmetry breaking limit, is ruled out by LEP2 constraints on chargino masses. The other class is potentially phenomenologically viable, however. Studying this latter class, we see that sparticle masses are rather similar: most sparticles' masses are within 1% of the standard solution's. The most constraining LHC searches (various jets plus missing transverse momentum searches) are unlikely to have a large difference between solutions: if a CMSSM point is ruled out by such an analysis in the standard solution, it will be also ruled out for the additional solution (and vice versa). However, chargino masses may be around 10% different between solutions and so any CMSSM LHC analyses relying on charginos in decay chains are vulnerable to correction coming from the existence of the multiple solutions. Indeed, branching ratios of decays of stops and sbottoms into charginos are shown to differ by several tens of percent. Precision measurements at a future linear collider facility could certainly be sensitive to percent or per-mille differences in various sparticle masses, and so exclusion or measurement would need to take the additional solutions into account.

We predicted the thermal relic density of neutralinos, comparing the standard and the new, phenomenologically viable class of solutions. Here, we see large differences: a factor of 2–3 in  $\Omega_{\text{CDM}}h^2$  is possible between the predictions of the two separate solutions. We have illustrated with a point that predicts far too much dark matter for the standard solution, where nevertheless the additional solution is near the observational central value derived by Planck. Thus, we conclude that analyses involving  $\Omega_{\text{CDM}}h^2$  as a constraint should, of necessity, take multiple solutions into account. Many recent CMSSM analyses fit  $\Omega_{\text{CDM}}$  and other data (see, for example [35–40]), and these should be modified to include the additional solutions. It could be, for instance, that a better best-fit point exists within the additional solutions, meaning that the  $\chi^2$  fit frequentist type analyses' 95% confidence level contours move significantly.

## Acknowledgements

This work has been partially supported by STFC. DG is funded by a Herchel Smith fellowship. We would like to thank other members of the Cambridge SUSY Working Group for discussions and helpful comments.

## A Definition of Quantities in the Boundary Conditions

Here, we define the quantities appearing in Table 2. Running quantities without a 'pred' label are obtained by running the initial parameters down in renormalisation scale from  $V_{11}$ . The other quantities in  $f_1$  and  $f_2$  come from the electroweak symmetry breaking conditions, i.e.

$$M_Z(\text{pred})^2 = 2 \left( \frac{m_{H_1}^2(V_{11}) - m_{H_2}^2(V_{11}) \tan^2 \beta(V_{11})}{\tan^2 \beta(V_{11}) - 1} - \mu^2(V_{11}) \right) + \Pi_{ZZ}^T(V_{11}), \quad (\text{A.1})$$

where in practice, we use  $\Pi_{ZZ}^T(V_{11}) = M_Z(\text{exp})^2 - M_Z^2(V_{11})$  for the self energy of the  $Z$  boson,  $M_Z^2(V_{11}) = v^2(V_{11})[g_2^2(V_{11}) + \frac{3}{5}g_1^2(V_{11})]/2$  and

$$\tan \beta^{\text{pred}}(V_{11}) = \tan \frac{1}{2} \left[ \sin^{-1} \left( \frac{2m_3^2(V_{11})}{m_{\tilde{H}_1}^2(V_{11}) + m_{\tilde{H}_2}^2(V_{11}) + 2\mu^2(V_{11})} \right) \right]. \quad (\text{A.2})$$

$m_{\tilde{H}_i}^2 = m_{H_i}^2 - t_i/v_i$  are fixed by the soft SUSY breaking mass parameters for the Higgs fields  $m_{\tilde{H}_i}^2$ ,  $i \in \{1, 2\}$ , as well as by the tadpole contributions  $t_i$  coming from loops. In  $f_3$ ,  $M_{\text{SUSY}}^{\text{pred}} = \sqrt{m_{\tilde{t}_1}(V_{11})m_{\tilde{t}_2}(V_{11})}$ . The MSSM parameters are then evolved to  $M_Z(\text{exp})$ , where the  $M_Z$  boundary conditions are applied: in  $f_{4,5,6}$ ,  $Y_{t,b,\tau}^{\text{pred}}(M_Z(\text{exp}))$  are the top, bottom and tau Yukawa couplings predicted by the central values of the top, bottom and tau pole masses, respectively, once all of the SUSY contributions have been added to the pole masses  $m_{t,b,\tau}$  [16]:

$$\begin{aligned} Y_t^{\text{pred}}(M_Z(\text{exp})) &= \frac{\sqrt{2}(m_t + \Re\Sigma_t)}{v(M_Z(\text{exp})) \sin \beta(M_Z(\text{exp}))}, \\ Y_{b,\tau}^{\text{pred}}(M_Z(\text{exp})) &= \frac{\sqrt{2}(m_{b,\tau} + \Re\Sigma_{b,\tau})}{v(M_Z(\text{exp})) \cos \beta(M_Z(\text{exp}))}, \end{aligned} \quad (\text{A.3})$$

where  $\Re\Sigma_{t,b,\tau}$  are the real parts of the one-loop MSSM contributions to the top, bottom and tau masses, respectively.  $g_3^{\text{pred}}(M_Z(\text{exp}))$  in  $f_9$  is extracted from the central value of  $\alpha_s(M_Z)$  in the  $\overline{MS}$  scheme by changing to the modified DRED scheme and adding MSSM contributions and  $g_{1,2}^{\text{pred}}(M_Z(\text{exp}))$  in  $f_{7,8}$  are the gauge couplings predicted by the central values of  $\alpha(M_Z(\text{exp}))$  and the Fermi constant  $G_F$  in the manner described in Appendix D of Ref. [16].  $f_{10}$ , contains the boundary condition on the Higgs VEV, where

$$v^{\text{pred}2} = 4 \frac{M_Z(\text{exp})^2 + \Pi_{ZZ}^T(V_{11})}{g_2^2(V_{11}) + \frac{3}{5}g_1^2(V_{11})} \quad (\text{A.4})$$

and all Higgs vacuum expectation values (VEVs) are in the Feynman gauge (as are the loop corrections), and  $v^2$  is the Pythagorean combination of the two MSSM Higgs VEVs, i.e.  $v_1^2 + v_2^2$ . In  $f_{11}$ ,  $\tan \beta$  refers to the value that is input and specifies the CMSSM parameter point.

## References

- [1] P. Fayet, *Supersymmetry and Weak, Electromagnetic and Strong Interactions*, *Phys.Lett.* **B64** (1976) 159.
- [2] P. Fayet, *Spontaneously Broken Supersymmetric Theories of Weak, Electromagnetic and Strong Interactions*, *Phys.Lett.* **B69** (1977) 489.
- [3] G. R. Farrar and P. Fayet, *Phenomenology of the Production, Decay, and Detection of New Hadronic States Associated with Supersymmetry*, *Phys.Lett.* **B76** (1978) 575–579.
- [4] P. Fayet, *Relations Between the Masses of the Superpartners of Leptons and Quarks, the Goldstino Couplings and the Neutral Currents*, *Phys.Lett.* **B84** (1979) 416.



- [5] S. Dimopoulos and H. Georgi, *Softly Broken Supersymmetry and SU(5)*, *Nucl.Phys.* **B193** (1981) 150.
- [6] B. Allanach, D. P. George and B. Gripaios, *The dark side of the  $\mu$ : on multiple solutions to renormalisation group equations, and why the CMSSM is not necessarily being ruled out*, *JHEP* **1307** (2013) 098 [[1304.5462](#)].
- [7] N. Arkani-Hamed, G. L. Kane, J. Thaler and L.-T. Wang, *Supersymmetry and the LHC inverse problem*, *JHEP* **0608** (2006) 070 [[hep-ph/0512190](#)].
- [8] B. Allanach and M. J. Dolan, *Supersymmetry With Prejudice: Fitting the Wrong Model to LHC Data*, *Phys.Rev.* **D86** (2012) 055022 [[1107.2856](#)].
- [9] M. Drees and M. M. Nojiri, *Radiative symmetry breaking in minimal  $N = 1$  supergravity with large Yukawa couplings*, *Nucl.Phys.* **B369** (1992) 54–98.
- [10] B. Allanach, *SOFTSUSY: a program for calculating supersymmetric spectra*, *Comput.Phys.Commun.* **143** (2002) 305–331 [[hep-ph/0104145](#)].
- [11] H. Baer, F. E. Paige, S. D. Protopopescu and X. Tata, *Simulating Supersymmetry with ISAJET 7.0 / ISASUSY 1.0*, [hep-ph/9305342](#).
- [12] W. Porod, *SPheno, a program for calculating supersymmetric spectra, SUSY particle decays and SUSY particle production at  $e^+ e^-$  colliders*, *Comput.Phys.Commun.* **153** (2003) 275–315 [[hep-ph/0301101](#)].
- [13] A. Djouadi, J.-L. Kneur and G. Moultaka, *SuSpect: A Fortran code for the supersymmetric and Higgs particle spectrum in the MSSM*, *Comput.Phys.Commun.* **176** (2007) 426–455 [[hep-ph/0211331](#)].
- [14] G. Teschl, *Ordinary Differential Equations and Dynamical Systems*. American Mathematical Society, 2012.
- [15] D. Capper, D. Jones and P. van Nieuwenhuizen, *Regularization by Dimensional Reduction of Supersymmetric and Nonsupersymmetric Gauge Theories*, *Nucl.Phys.* **B167** (1980) 479.
- [16] D. M. Pierce, J. A. Bagger, K. T. Matchev and R.-j. Zhang, *Precision corrections in the minimal supersymmetric standard model*, *Nucl.Phys.* **B491** (1997) 3–67 [[hep-ph/9606211](#)].
- [17] D. Chowdhury, R. Garani and S. K. Vempati, *SUSEFLAV: Program for supersymmetric mass spectra with seesaw mechanism and rare lepton flavor violating decays*, *Comput.Phys.Commun.* **184** (2013) 899–918 [[1109.3551](#)].
- [18] R. Bellman, *Dynamic programming*. Princeton University Press, 1957.
- [19] W. Press, S. Teukolsky, W. Vetterling and B. Flannery, *Numerical Recipes in C.: Second Edition*. Cambridge University Press, 1992.
- [20] C. Broyden, *A Class of Methods for Solving Nonlinear Simultaneous Equations*, *Mathematics of Computation* **19** (1965) 577.
- [21] **ATLAS** Collaboration, G. Aad *et. al.*, *Search for squarks and gluinos with the ATLAS detector in final states with jets and missing transverse momentum using  $4.7 \text{ fb}^{-1}$  of  $\sqrt{s} = 7$  TeV proton-proton collision data*, *Phys.Rev.* **D87** (2013) 012008 [[1208.0949](#)].
- [22] **CMS** Collaboration, S. Chatrchyan *et. al.*, *Search for new physics in the multijet and missing transverse momentum final state in proton-proton collisions at  $\sqrt{s} = 7$  TeV*, *Phys.Rev.Lett* **109** (2013) 171803 [[1207.1898](#)].



- [23] G. Aad *et al.*, *Search for squarks and gluinos with the ATLAS detector in final states with jets and missing transverse momentum and  $20.3 \text{ fb}^{-1}$  of  $\sqrt{s} = 8 \text{ TeV}$  proton-proton collision data*, Tech. Rep. ATLAS-CONF-2013-047, CERN, Geneva, May, 2013.
- [24] LEPSUSYWG, ALEPH, DELPHI, L3 and OPAL experiments, *note LEPSUSYWG/01-03.1* (<http://lepsusy.web.cern.ch/lepsusy/Welcome.html>).
- [25] **Particle Data Group** Collaboration, J. Beringer *et al.*, *Supersymmetry, Part I (theory)*, *Phys.Rev.* **D86** (2012) 0100001.
- [26] **ATLAS** Collaboration, G. Aad *et al.*, *Observation of a new particle in the search for the Standard Model Higgs boson with the ATLAS detector at the LHC*, *Phys.Lett.* **B716** (2012) 1–29 [[1207.7214](#)].
- [27] **CMS** Collaboration, S. Chatrchyan *et al.*, *Observation of a new boson at a mass of 125 GeV with the CMS experiment at the LHC*, *Phys.Lett.* **B716** (2012) 30–61 [[1207.7235](#)].
- [28] B. Allanach, J. Blaising, K. Desch, J. Ellis, G. Giudice, C. Grefe, S. Kraml, T. Lastovicka, L. Linssen, J. Marschall, S. Martin, A. Muennich, S. Poss, P. Roloff, F. Simon, J. Strube, M. Thomson and J. Wells, *The physics benchmark processes for the detector performance studies used in CLIC CDR Volume 3*, .
- [29] P. Z. Skands, B. Allanach, H. Baer, C. Balazs, G. Belanger *et al.*, *SUSY Les Houches accord: Interfacing SUSY spectrum calculators, decay packages, and event generators*, *JHEP* **0407** (2004) 036 [[hep-ph/0311123](#)].
- [30] A. Djouadi, M. Muhlleitner and M. Spira, *Decays of supersymmetric particles: The Program SUSY-HIT (SUspect-SdecaY-Hdecay-InTerface)*, *Acta Phys.Polon.* **B38** (2007) 635–644 [[hep-ph/0609292](#)].
- [31] A. P. G. Belanger, F. Boudjema and A. Semenov, *micrOMEGAs2.0: A program to calculate the relic density of dark matter in a generic model*, *Comput.Phys.Commun.* **176** (2007) 367 [[0211331](#)].
- [32] A. P. G. Belanger, F. Boudjema and A. Semenov, *Dark matter direct detection rate in a generic model with micrOMEGAs2.1*, [0803.2360](#).
- [33] Y. Bai, H.-C. Cheng, J. Gallicchio and J. Gu, *A Toolkit of the Stop Search via the Chargino Decay*, *JHEP* **1308** (2013) 085 [[1304.3148](#)].
- [34] **Planck** Collaboration, P. Ade *et al.*, *Planck 2013 results. XVI. Cosmological parameters*, [1303.5076](#).
- [35] B. Allanach and C. Lester, *Multi-dimensional mSUGRA likelihood maps*, *Phys.Rev.* **D73** (2006) 015013 [[hep-ph/0507283](#)].
- [36] O. Buchmueller, R. Cavanaugh, A. De Roeck, M. Dolan, J. Ellis *et al.*, *Higgs and Supersymmetry*, *Eur.Phys.J.* **C72** (2012) 2020 [[1112.3564](#)].
- [37] C. Balazs, A. Buckley, D. Carter, B. Farmer and M. White, *Should we still believe in constrained supersymmetry?*, [1205.1568](#).
- [38] M. E. Cabrera, J. A. Casas and R. R. de Austri, *The health of SUSY after the Higgs discovery and the XENON100 data*, [1212.4821](#).
- [39] A. Fowlie, M. Kazana, K. Kowalska, S. Munir, L. Roszkowski *et al.*, *The CMSSM Favoring New Territories: The Impact of New LHC Limits and a 125 GeV Higgs*, *Phys.Rev.* **D86** (2012) 075010 [[1206.0264](#)].

- [40] C. Strege, G. Bertone, F. Feroz, M. Fornasa, R. R. de Austri *et. al.*, *Global Fits of the  $cMSSM$  and  $NUHM$  including the LHC Higgs discovery and new XENON100 constraints*, *JCAP* **1304** (2013) 013 [[1212.2636](#)].